A contact-based constitutive model for the numerical analysis of masonry structures using the distinct element method

Oktiovan, Y. P.; Messali, F.; Pulatsu, B.; Lemos, J. V.; Rots, J. G.

DOI
10.1016/j.compstruc.2024.107499

Publication date
2024

Document Version
Final published version

Published in
Computers and Structures

Citation (APA)
Oktiovan, Y. P., Messali, F., Pulatsu, B., Lemos, J. V., & Rots, J. G. (2024). A contact-based constitutive model for the numerical analysis of masonry structures using the distinct element method. *Computers and Structures*, *303*, Article 107499. https://doi.org/10.1016/j.compstruc.2024.107499

Important note
To cite this publication, please use the final published version (if applicable).
Please check the document version above.

Computers and Structures 303 (2024) 107499

Contents lists available at ScienceDirect

Computers and Structures

journal homepage: www.elsevier.com/locate/compstruc

A contact-based constitutive model for the numerical analysis of masonry structures using the distinct element method

Y.P. Oktiovan [a,*], F. Messali [a], B. Pulatsu [b], J.V. Lemos [c], J.G. Rots [a]

[a] Faculty of Civil Engineering & Geosciences, Delft University of Technology, Stevinweg 1, 2628CN, Delft, Netherlands
[b] Department of Civil and Environmental Engineering, Carleton University, Ottawa, Canada
[c] National Laboratory for Civil Engineering (LNEC), Lisbon, Portugal

ARTICLE INFO

Keywords:
Masonry
Constitutive model
Distinct element method
Explicit integration scheme
Multi-surface plasticity
Damage mechanics

ABSTRACT

This study presents a robust contact constitutive model in the distinct element method (DEM) framework for simulating the mechanical behavior of masonry structures. The model is developed within the block-based modeling strategy, where the masonry unit is modeled as deformable blocks with potential crack surfaces in the middle of the bricks, while the mortar joints are defined as zero-thickness interfaces. The modeling strategy implements multi-surface plasticity with damage mechanics, including a tension cut-off, Coulomb failure criterion, and an elliptical compressive cap for the damage in tension, shear, and compression, respectively. Two new features are introduced in this contact model: a piecewise linear softening function for strength degradation in tension and shear and a hardening/softening function to phenomenologically define the compressive damage of masonry composite into the unit-mortar interface. The constitutive model is implemented in commercial DEM software using the small displacement configuration and validated against material and experimental tests on masonry walls subjected to constant pre-compression and monotonically increasing in-plane load. The experimental and numerical results regarding the force-displacement relationship and damage pattern produced by the proposed constitutive model are compared and critically discussed, demonstrating the capability of DEM coupled with the suitable constitutive law in simulating the behavior of masonry structures.

1. Introduction

Unreinforced masonry (URM) structures, considered one of the oldest forms of construction known to man, account for the majority of existing residential buildings and architectural heritage worldwide [1–4]. It is generally known that URM structures are capable of withstanding gravitational loads but are vulnerable to extraordinary actions, such as settlements, earthquakes, strong wind, etc. This prompts researchers to investigate the state of maintenance and the mechanical behavior of these URM structures further through numerical analyses and/or experiments.

The numerical investigation of the behavior of masonry structures itself has been an active field of research over the last half-century. With the rapid increase of computational power over the past few decades, researchers have opted for numerical modeling approaches that can efficiently predict nonlinear and complex responses of URM structures. D'Altri et al. [5] categorized the modeling strategies for masonry structures into four distinct groups: Block-based models where masonry units are modeled as rigid or deformable blocks with the unit-mortar interfaces defined either by interface elements, cohesive-frictional contact points, or textured continua [6–10]; Continuum models where masonry is defined as a continuum body with no distinction between the units and mortar joints, where either calibrated constitutive laws or homogenization procedures are applied to represent the discrete nature of masonry [11–15]; Equivalent frame models where the structure is idealized into panel structural elements with constitutive laws that reproduce the mechanical response of masonry as structural components instead of as masonry constituents in the continuum-based models [16–20]; and Geometry-based models where masonry structures, modeled as rigid bodies, are analyzed through limit-analysis-based solutions implementing static or kinematic theorems [21–25].

The constitutive model proposed in this paper is developed within the block-based modeling strategy. Most numerical strategies that follow the block-based models utilize a combination of damage and plasticity formulations to capture the failure and local mechanisms at the bond (also termed as unit-mortar interface) and within the masonry unit of

* Corresponding author.
E-mail address: y.p.oktiovan@tudelft.nl (Y.P. Oktiovan).

https://doi.org/10.1016/j.compstruc.2024.107499
Received 27 February 2024; Accepted 31 July 2024
Available online 6 August 2024

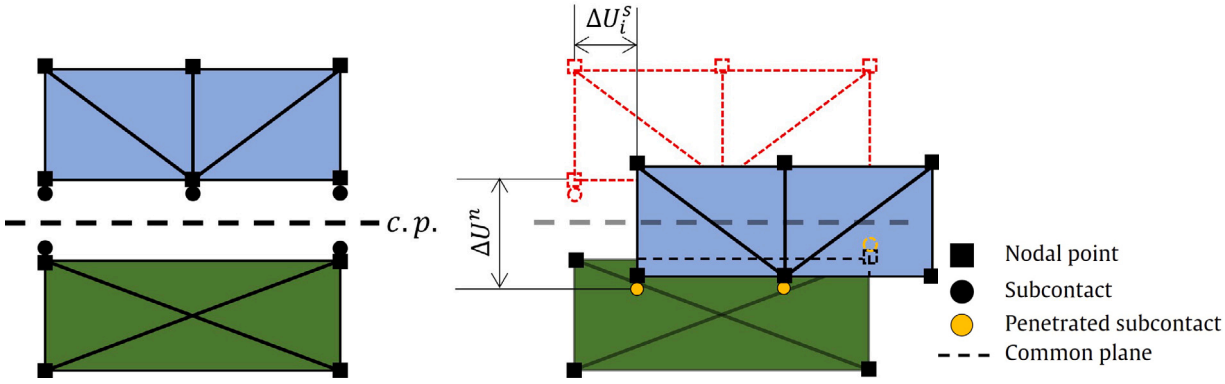

(a) Before interpenetration (b) After interpenetration

Fig. 1. Illustration of subcontacts of two deformable blocks in distinct element method.

URM structures. In the context of block-based modeling strategy with damaged plasticity concept, one of the earliest attempts at the development of the constitutive model was made by Lotfi and Shing [26], who proposed a single hyperbolic yield surface for the damage in shear and tension. Similar work was proposed by Lourenço and Rots [27], who introduced a multi-surface plasticity model with Coulomb-friction yield criterion for the shear region, tension cut-off, and an elliptical "cap" yield function for tension and compression regions, respectively. The interface model was then extended to account for stiffness degradation during cyclic loading [28]. Since then, many constitutive models have been developed incorporating the multi-surface plasticity concept within the block-based modeling strategy [9,29–34].

The constitutive models mentioned above were developed on finite element-based frameworks, which often rely on the implicit backward Euler method to iteratively solve the system's equilibrium. The implicit solver is known to encounter convergence issues and instabilities on highly nonlinear problems, e.g. the analysis of masonry structures. Therefore, researchers often opt for other solutions, such as the explicit integration method [35,36] or sequentially linear method [37], to simulate the failure mechanism of masonry structures.

In the last several decades, discontinuum analysis, based on the distinct element method (DEM), has gained increasing attention within the field of computational modeling of masonry structures as the numerical method is able to define the mechanical interaction between blocks through contact points and explicitly represent the typical brick and bond failure mechanisms such as cracking and sliding (see [6,7,38–42], etc.). The DEM, developed by Cundall [43], represents masonry as a system of rigid and/or deformable blocks by a set of cohesive-frictional contact points. The DEM utilizes the explicit time-marching integration scheme as the solution procedure, which is able to alleviate the convergence problems often found in numerical modeling with the implicit integration scheme [44].

The Mohr-Coulomb contact model is commonly employed in the DEM framework to analyze masonry structures. This model, utilized in various studies ([7,22,38,42,45]), accounts for brittle failure in tension and shear, although it simplifies the true mechanical response of masonry components. Furthermore, this constitutive model neglects the compression damage that often occurs at URM walls or structures with higher axial stress and/or aspect ratio [46]. Recently, more sophisticated contact constitutive models have been proposed in the literature to better address the post-peak response and coupled damage mechanisms between the compression-shear and tension-shear regimes, e.g. [39,47].

This paper introduces a new contact constitutive model to be utilized in the DEM framework using the multi-surface plasticity with the Coulomb friction failure criterion and tension cut-off to address the failure in shear and tension regions, respectively, and a compression cap to limit the failure in compression and combined shear-compression regions. The main contributions of this paper are the proposed contact constitutive model with post-peak behavior in tension and shear through the user-defined piecewise linear softening functions and the hardening/softening function in the compression regime. The piecewise linear softening functions allow flexible yet robust representations of damage in tension and shear, while the hardening/softening function creates the actual behavior of masonry composite when subjected to pure compression load. Robust force update routines for each failure regime within the explicit integration scheme are implemented to stabilize the system.

The proposed constitutive law is implemented as a user-defined contact constitutive model in *3DEC* [48], a commercial software. The proposed model is validated at the material and structural levels, including comparisons to other numerical methods, to demonstrate the capability of DEM with the suitable constitutive law for masonry analysis.

2. Computational background of the distinct element method

In this section, the computational procedure of DEM is briefly explained. This contact-based approach is developed under the explicit time-marching integration scheme to solve the equations of motion and obtain each block's relative velocities and displacements. The masonry units are represented as deformable blocks with linear elastic behavior. The deformability of the discrete blocks is introduced by discretizing them into constant-strain tetrahedral elements with three translational degrees of freedom at each node. Meanwhile, the mortar joints are defined as cohesive-frictional contact points [43]. It is important to note that the formulations explained herein, including the formulation of the contact constitutive model, are defined for small displacement configuration where contact points detected at the start of the simulation are kept throughout the simulation.

The 'common-plane' (CP) concept is used for the detection of blocks in contact, which is essentially a plane in which the maximum overlap between the two blocks is minimized. An illustration of the two deformable blocks in contact is presented in Fig. 1. The illustration is presented in two dimensions for simplicity, but the same logic applies in the three-dimensional implementation of the detection algorithm. Furthermore, for the simplification of the definition of CP, rigid translation without any rotation is assumed for the blue block in Fig. 1b. This implies that equal velocity is imposed on the subcontacts in the blue block. In reality, incremental rotation can occur, causing the unit normal to the CP for each subcontact to differ, resulting in different displacement increments.

Once the gap, measured from the unit normal to the CP, between the two deformable blocks is lesser than the tolerance, the blocks are assumed to be in contact. The contact points (hereby termed subcontacts)

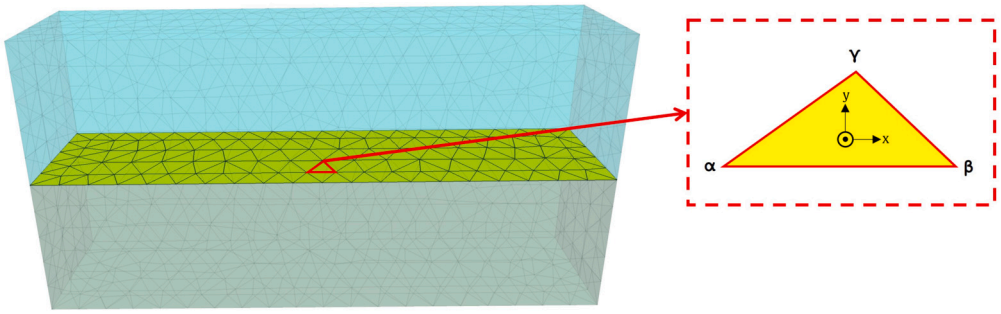

Fig. 2. Local coordinates of contacting faces between two blocks.

are then defined on both blocks (the black circles in Fig. 1), comprising normal and shear springs that relate the relative displacements to the subcontact forces. For the case of Fig. 1a, the subcontacts are created for each node on the contacting faces. If both blue and green blocks are moving with a nodal velocity of V_i^B and V_i^G, respectively, the relative velocity for the vertex in the blue block is shown in Eq. (1). The V_i^G term comes first for the relative velocity in the green block.

$$V_i = V_i^B - V_i^G \tag{1}$$

If the green block is stationary (as the case for Fig. 1b), the opposing velocity V_i^G is equal to zero. The relative displacement increment at the subcontact in the blue block ΔU_i is then calculated in Eq. (2).

$$\Delta U_i = V_i \Delta t \quad \text{where} \quad u_i^{t+} = u_i^{t-} + \Delta U_i \tag{2}$$

where Δt is the timestep, u_i^{t+} and u_i^{t-} are the nodal displacement vectors at the time $t + \Delta t/2$ and $t - \Delta t/2$, respectively. This displacement increment along the CP is then resolved into normal and shear components, ΔU^n and ΔU_i^s respectively, as given in Eq. (3).

$$\Delta U^n = \Delta U_i n_i \quad \text{and} \quad \Delta U_i^s = \Delta U_i - \Delta U_j n_j n_i \tag{3}$$

where n is the unit normal that points from the blue block to the green block, and i and j are vector indices with values from 1 to 3, denoting the vector components in the global coordinate system. The subcontact force in normal and shear are then defined in Eqs. (4) and (5), respectively, under the linear elastic law [48].

$$F^n := F^n + \Delta F^n \quad \text{where} \quad \Delta F^n = k_n A_c \Delta U^n \tag{4}$$

$$F_i^s := F_i^s + \Delta F_i^s \quad \text{where} \quad \Delta F_i^s = k_s A_c \Delta U_i^s \tag{5}$$

where k_n and k_s are the normal and shear stiffnesses, respectively, and A_c is the subcontact area, calculated as 1/3 of the triangular faces' areas where the subcontact lies. This area is halved for face-to-face contact or coinciding blocks, as the subcontacts are defined for vertices of both blocks that occupy the same exact position in space. The subcontact force vector is given by Eq. (6)

$$F_i^c = F^n n_i + F_i^s \tag{6}$$

where n_i is the unit normal to the contacting bodies (points, edges, or surfaces).

For deformable blocks configuration, the subcontact force in Eq. (6) is added directly to the nodal points. For face-to-face contact (Fig. 2), the subcontact force is distributed among the three vertices that form a face (α, β, γ) using weight factors, as presented in Eq. (7).

$$F_i^\alpha := F_i^\alpha \pm F_i^c W_\alpha \qquad F_i^\beta := F_i^\beta \pm F_i^c W_\beta \qquad F_i^\gamma := F_i^\gamma \pm F_i^c W_\gamma \tag{7}$$

where W_α, W_β, and W_γ are the weight factors for vertices α, β, and γ, respectively. These weight factors are defined according to a local coordinate system with one local axis normal to the face plane. This is defined in Eq. (8) for vertex α, while W_β and W_γ are calculated by circular permutation of the superscripts in Eq. (8).

$$W_\alpha = \frac{Y^\gamma X^\beta - Y^\beta X^\gamma}{(X^\alpha - X^\gamma)(Y^\beta - Y^\gamma) - (Y^\alpha - Y^\gamma)(X^\beta - X^\gamma)} \tag{8}$$

where X and Y denote the local in-plane coordinates of each vertex.

The subcontact force in Eq. (6), along with external load (F^l), gravitational force (F^g), and the force due to internal stress of the discretized deformable blocks (F^z), form the total force (F_i), as shown in Eq. (9).

$$F_i = F_i^z + F_i^c + F_i^l + F_i^g \tag{9}$$

As a deformable block is divided into a mesh of tetrahedral elements (see Fig. 1a), the F_i^z is a nodal force vector equivalent to the stresses in the tetrahedral elements converging on the node under consideration. Meanwhile, the gravitational force F_i^g is simply the gravitational constant multiplied by the lumped mass at the nodal point, which is the sum of one-third of the tetrahedral masses connected to the gridpoint.

The subcontact force vector in Eq. (6) only exists at the nodal points along the block boundary. This force vector equals zero at nodal points outside of the block boundary. The total force contributes to the equation of motion for the system. The equation of motion is presented in Eq. (10), where the total nodal force is zero at equilibrium.

$$\dot{u}_i^{t+} = \dot{u}_i^{t-} + \left(\Sigma F_i^t - F_i^d\right) \frac{\Delta t}{m} \tag{10}$$

where $\dot{u}_i^{t+}$ and $\dot{u}_i^{t-}$ (essentially V_i^{t+} and V_i^{t-}) are the nodal velocity vector at the time $t + \Delta t/2$ and $t - \Delta t/2$, respectively, m is the nodal mass, and F_i^d is the nodal damping force, defined in Eq. (11).

$$F_i^d = \alpha |F_i^t| sgn(\dot{u}_i^{t-}) \tag{11}$$

The damping force is based on a proportion of the total force, controlled by a non-dimensional damping constant α set equal to 0.8, and the direction of the velocity vector (owned by the sign function). The adopted damping formulation, referred to as local damping [49], provides fast convergence to obtain quasi-static solutions. Once the nodal velocity in Eq. (10) is obtained, the nodal displacement is calculated again through Eq. (2). This is then used again to update the normal and shear subcontact forces, which are adjusted according to the assigned contact constitutive law.

The whole process is summarized in Fig. 3. The solution procedure at one node described above is iterated until either equilibrium or failure is reached. Failure in the context of an explicit integration scheme is defined as the condition where the evaluated node is unable to find a steady-state flow as it accelerates to infinity.

The numerical procedure under the distinct element method is already implemented in a commercial three-dimensional discrete element code, called *3DEC*, developed by Itasca [48]. It is important to note that the explicit time marching integration scheme used for the distinct element method is conditionally stable, as it is typical for other methods using the explicit solver [44]. The time step required to achieve stability in calculating the internal block deformation is defined in Eq. (12) [50].

$$\Delta t_{block} = 2\sqrt{\frac{m_i}{k_{n,i} + k_{tet,i}}} \tag{12}$$

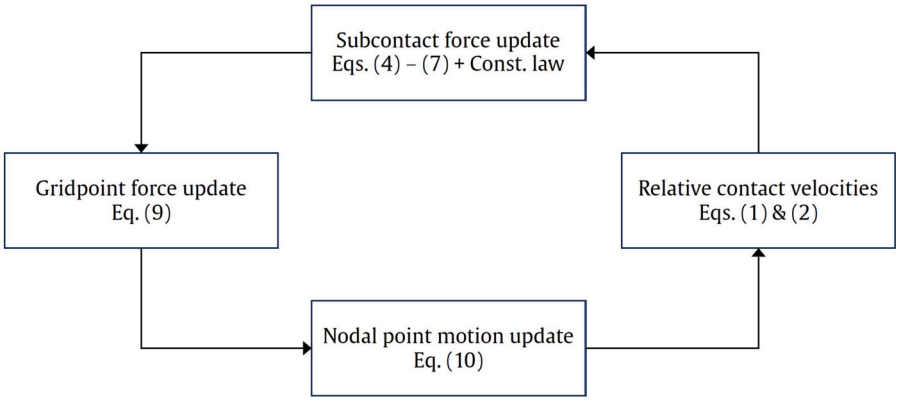

Fig. 3. Calculation cycle in DEM [48].

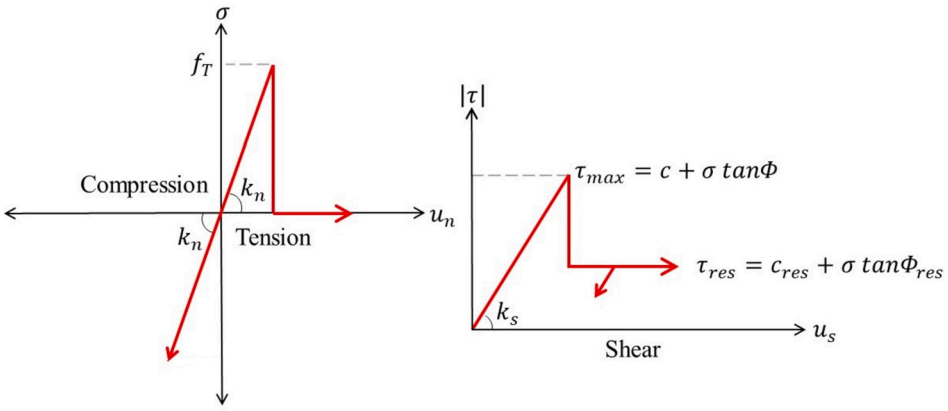

Fig. 4. Standard Mohr-Coulomb contact model available in 3DEC [8].

where t_{block} is the timesteps requirement for the calculation of block deformation, m_i is the mass of the blocks associated with node i, $k_{n,i}$ is the contact stiffness for nodes located on block boundary (zero for non-boundary nodes), $k_{tet,i}$ is the contributions of the stiffness of all blocks connected to node i, defined in Eq. (13).

$$k_{tet,i} = \frac{8}{3}\left(K + \frac{4}{3}G\right)\frac{l_{max}^2}{h_{min}} \tag{13}$$

where K and G are the block's bulk and shear moduli, respectively, l_{max} is the longest block length, and h_{min} is the minimum height of the tetrahedron. The expression in Eq. (12) gives a conservative estimate based on an upper bound of the highest system eigenfrequency [51]. The estimate has been shown to be sufficiently stable even for complex nonlinear systems [52,53].

3. Contact constitutive model

While the behavior of the contact points can be represented using Eqs. (4) and (5) under linear elastic law, the failure progression of the contact points under shear, tensile, and compressive regimes needs to be properly defined to obtain numerical responses that represent the actual condition of masonry structures. The contact constitutive law suitable for masonry structures and readily available within the commercial distinct element code [48] is the Mohr-Coulomb contact model, in which a cohesive-frictional contact law is defined and limited by a tension cut-off, as presented in Fig. 4.

Under the Mohr-Coulomb contact model, the tensile strength drops to zero at the onset of failure, while the shear strength drops to the residual strength. While this model is typically sufficient to provide a decent prediction of the ultimate capacity of masonry structures that exhibit brittle behavior [7,38,42,54–56], an accurate definition of the post-peak behavior for the tensile and shear regime is essential to represent the damage initiation and propagation of masonry structures [47]. Furthermore, this contact constitutive model considers the damage that occurs only in tension and shear regimes and assumes an infinite strength in the compressive regime, as presented in Fig. 4. In reality, compression damage in the form of crushing at the compressed toes is often observed at URM walls or structures, especially those with higher axial stresses or aspect ratio [46,57].

Elasto-softening contact models were recently proposed to capture the post-peak behavior under tensile and shear regimes [39], which was extended to include the limit in the compressive regime through an elliptical compressive cap [58]. However, linear softening functions were adopted by the authors to define the tensile, shear, and compressive uniaxial behavior, which deviates from the nonlinear mechanism exhibited by the damaged masonry structures.

To overcome such limitations, the proposed contact constitutive model uses the damage plasticity concept to represent masonry structures with complex nonlinearities. It is important to note that the contact constitutive model introduced in this paper is developed within the small displacement theory, in which the contact points detected at the beginning of the analysis are used throughout the simulation. This is done to avoid spurious contact interpenetration and when compressive crushing occurs, which happens when the simulation is run under the large displacement theory.

The explanation of the constitutive model is divided into three stages: a definition of the plastic yield functions in Section 3.1, an explanation of the damage evolution law in Section 3.2, and an explanation of the stabilization process for the numerical strategy when damage has occurred in Section 3.3.

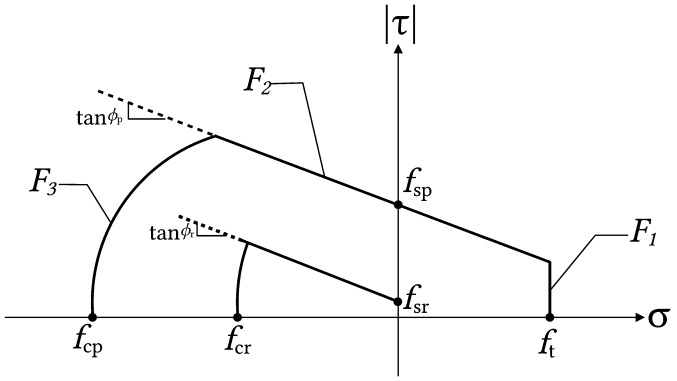

Fig. 5. Two-dimensional yield surfaces in normal stress vs shear stress space.

3.1. Plasticity definition of the interface

The proposed contact model uses the multi-surface plasticity concept illustrated in Fig. 5. The yield functions are mathematically defined in Eq. (14). The yield function consists of three regions as an extended version of the Coulomb-slip model: a tension cut-off region represented by F_1 (Eq. (14a)), the Coulomb-slip region defined in F_2 (Eq. (14b)), and an elliptical curve to control the behavior under shear-compression shown in F_3 (Eq. (14c)).

$$F_1 = \sigma - f_t(u_n^t) \tag{14a}$$

$$F_2 = |\tau| + \sigma \tan\phi(u_s) - f_s(u_s) \tag{14b}$$

$$F_3 = C_{nn}\,\sigma^2 + Css\,|\tau|^2 + C_n\,\sigma - f_c^2(u_n^c) \tag{14c}$$

where u_n^c and u_n^t are the relative normal subcontact displacement in compression and tension, respectively, σ is the normal stress, τ is the shear stress, $\phi(u_s)$ is the friction angle correlated to the shear displacement, $f_t(u_n^t)$ is the tensile strength that evolves in accordance with the positive normal displacement, $f_s(u_s)$ is the cohesive strength correlated to the shear displacement, $f_c(u_n^c)$ is the compressive strength that evolves in accordance with the negative normal displacement, C_{nn} and C_{ss} are the parameters that control the radius of the elliptical curve in Fig. 5 in normal and shear directions, respectively, and C_n is the ellipsis center.

The yield functions F_1 and F_2 are identical to those implemented in the Coulomb-slip contact model. The elliptical yield surface F_3 is the compression cap adopted from Lourenço and Rots [27]. An associated flow rule is assumed for the tensile cut-off and compression cap regions where plastic potential G_1 and G_3 are set equal to F_1 and F_3, respectively. Meanwhile, the non-associated flow rule is used for the F_2 yield surface to address the role of dilatancy at the onset of damage in the mortar joints [31,56,59]. The mathematical expression of the plastic potential G_2 is defined in Eq. (15).

$$G_2 = |\tau| + \sigma \tan\psi - f_s(u_s) \tag{15}$$

where ψ is the dilation angle. van Zijl [31], Chainmoon [60], and Li & Zeng [61] showed that the dilation angle also softens as the shear load increases, similar to the friction angle. However, the dilatancy softening is not considered in the current implementation of the contact constitutive model, and the dilatancy angle set for the numerical analysis in this research is equal to zero, similar to the values considered by other numerical approaches [27,30,58]

3.2. Damage evolution law

The separation of the damage parameters is essential in modeling the contact constitutive model since the masonry interfaces behave differently when subjected to different modes of deformation, as presented in Fig. 6 at the masonry couplet level. The failure modes presented in Figs. 6a and 6d relate to the failure modes at the interface level, while Figs. 6b and 6e relate to the failure of the masonry constituents (units and mortar layers). The diagonal cracking failure presented in Fig. 6c combines failure at both units and interface levels. Similar failure modes can be observed when the problem scales up to masonry walls, as classified by Mann and Müller [62].

The strength degradation of the contact points during material softening is controlled by three damage parameters corresponding to tensile (d_t), shear (d_s), and compressive damage (d_c). In the proposed contact constitutive model, the tensile and shear softening behaviors are defined by a set of linear segments that reduce until the residual strength of each regime is reached. This formulation is an extension of the contact constitutive model proposed in the two-dimensional distinct element modeling by Lemos and Sarhosis [41].

A similar approach to Pulatsu et al. [63] is taken where the coupling between the tension and shear softening is assumed. The coupling process is obtained by combining the strength degradation in the forms of damage parameters in tension and shear (d_t and d_s, respectively) into a combined tensile/shear damage parameter d_{ts}. The user-defined values for both tensile and damage parameters are separated, while the combined damage parameter is calculated in the algorithm through Eq. (16).

$$d_{ts} = d_t(\bar{u_n}) + d_s(\bar{u_s}) - (d_t(\bar{u_n})d_s(\bar{u_s})) \tag{16}$$

The behavior of the proposed contact constitutive model is shown in Fig. 7. The mathematical formulation will be explained in the following sections.

3.2.1. Damage in tension

Under damage in tension, the tensile damage parameter d_t is a user-defined value that depends on the normal displacement ratio, defined in Eq. (17).

$$\bar{u}_n = \frac{u_n^t}{u_{np,t}} \quad \text{where} \quad u_{np,t} = \frac{f_t}{k_n} \tag{17}$$

Once damage occurs in tension, the evolution of the tensile stress is given by Eq. (18) as a function of the normal displacement ratio, where f_t is the peak tensile strength (also used in Eq. (17) and Fig. 5).

$$f_t(u_n^t) = f_t(1 - d_{ts}) \tag{18}$$

The combined damage parameter d_{ts} is given in Eq. (16). The damage parameter is defined by a table of pairs ($\bar{u_n}$, d_t), where $\bar{u_n}$ begins at 1 at the peak and decreases to zero at the residual state, while d_t starts at zero at the peak and increases to 1 at the residual state. The tabulated values of the damage parameters enable the user to approximate any given shapes of the post-peak softening curve in tension using a piecewise linear function. Maintaining the increasing damage parameter ensures a consistent assignment of numerical values to the scalar, which aligns with the conventional approach in damage-based models.

The tensile uniaxial behavior of the contact model is shown in Fig. 7a. With the presence of experimental data, e.g., mode I tensile tests [64], the post-peak stress-displacement experimental curve can be converted into joint displacement ratio and damage scalar pairs through Eqs. (17) and (18), respectively by assuming zero contribution from the shear regime on the combined damage parameter d_{ts}.

3.2.2. Damage in shear

The formulation for the strength degradation in the shear regime is similar to that defined for the tensile behavior, where the shear damage parameter is controlled by the normalized softening curve that depends on the joint shear displacement ratio, as shown in Eq. (19).

$$\bar{u}_s = \frac{u_s}{u_{sp}} \tag{19}$$

where u_{sp} is the displacement at peak shear strength, defined in Eq. (20).

$$u_{sp} = \frac{\tau_p}{k_s} \tag{20}$$

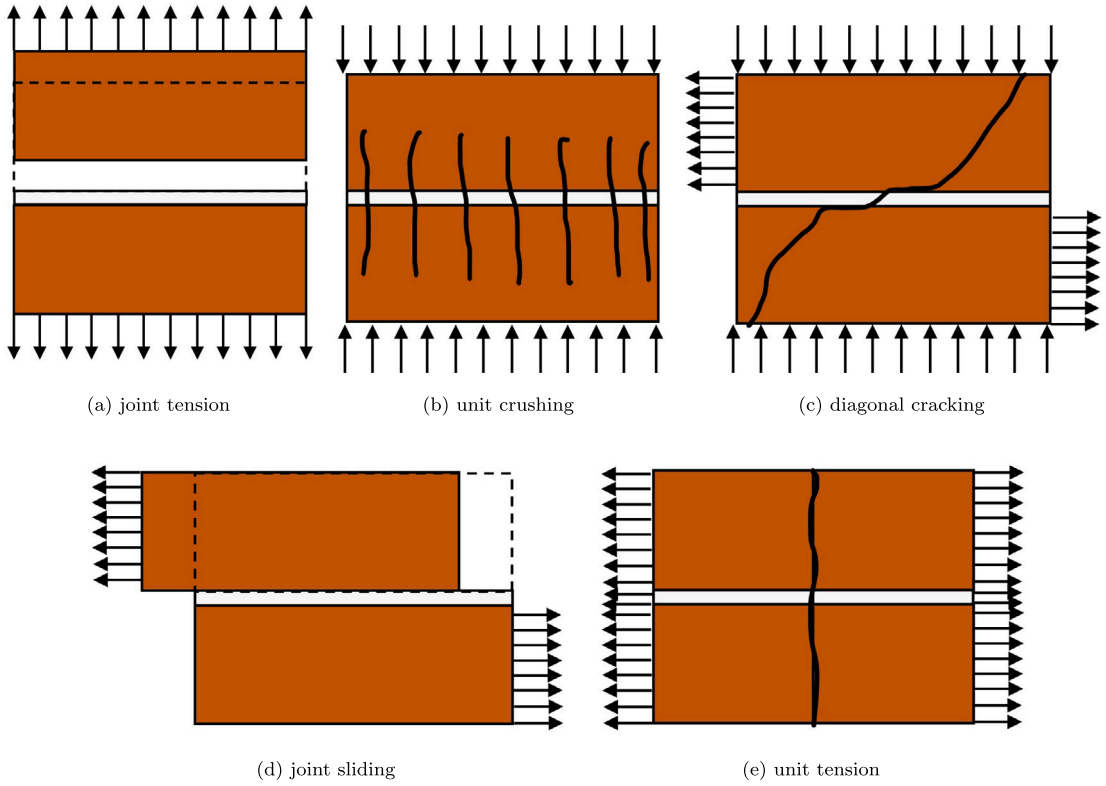

Fig. 6. Typical failure modes in masonry.

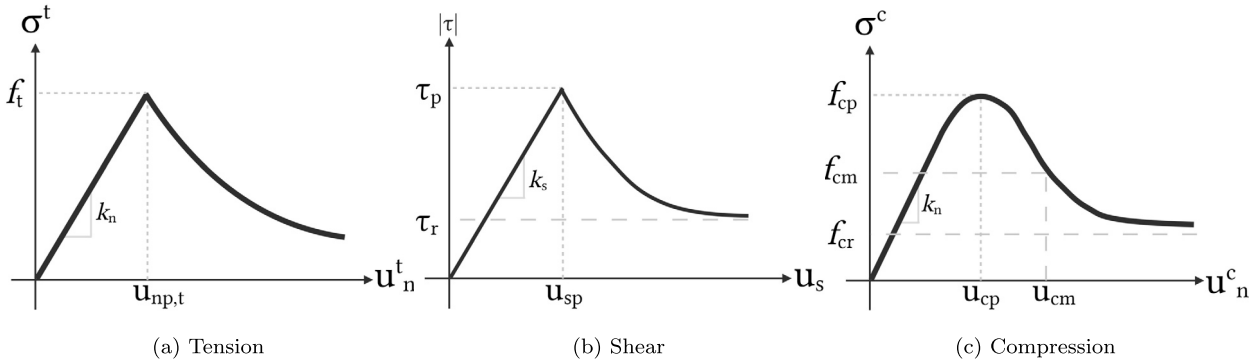

Fig. 7. Contact constitutive model behavior under each failure regime.

where τ_p is the peak shear strength formally defined in Eq. (21).

$$\tau_p = c_p - \sigma \tan(\phi_p) \tag{21}$$

where c_p and ϕ_p are the peak cohesion strength and friction angle, respectively.

The post-peak shear strength is formulated according to the Mohr-Coulomb envelope where the cohesion c and the friction angle depend on a user-defined shear damage parameter d_s, as shown in Eq. (22).

$$\tau(\bar{u}_s) = c(\bar{u}_s) - \sigma \tan(\phi)(\bar{u}_s) \tag{22}$$

where $c(\bar{u}_s)$ and $\tan(\phi)(\bar{u}_s)$ are the post-peak cohesion and friction angle, respectively. Equations for $c(\bar{u}_s)$ and $\tan(\phi)(\bar{u}_s)$ are respectively shown in Eqs. (23) and (24).

$$c(\bar{u}_s) = c_r + (c_p - c_r)(1 - d_{ts}) \tag{23}$$

$$\tan(\phi)(\bar{u}_s) = \tan(\phi_r) + (\tan(\phi_p) - \tan(\phi_r))(1 - d_{ts}) \tag{24}$$

Once again, the combined damage parameter is given in Eq. (16). Similar to the formulation in the tension regime, the user-defined value for the damage parameter comprises a table of pairs ($\bar{u_s}$, d_s) where $\bar{u_s}$ starts at 1 at peak and reduces to zero at residual state while d_s starts at zero at peak and increases to 1 at residual state. The behavior of the contact constitutive model under shear is presented in Fig. 7b.

Similar to the tensile regime, with the presence of experimental data, e.g., couplet or triplet tests, the post-peak stress-displacement curve from the experimental test can be converted into the joint displacement ratio and damage scalar through Eqs. (19), (23) and (24), by assuming zero contributions from the tensile regime to the combined damage parameter d_{ts}.

3.2.3. Damage in compression

The behavior of the contact constitutive model under compression is governed by a hardening/softening law, as presented in Fig. 7c. The initial linear-elastic phase for a typical masonry composite under

compression was observed between 30% to 40% of the compressive strength [65]. The hardening phase follows immediately after the linear-elastic phase before reaching the peak compressive strength. Mathematically, the hardening phase is defined by a parabolic function [27,66], presented in Equation (25).

$$\sigma_c(u_n^c) = \sigma_{el} + (f_{cp} - f_{c;el})\sqrt{\frac{2u_{inel}}{u_{cp}} - \frac{u_{inel}^2}{u_{cp}}} \tag{25}$$

where $\sigma_c(u_n^c)$ is the current compressive stress during the hardening phase, $f_{c;el}$ is the elastic compressive stress (set at 30% of the compressive strength by default), f_{cp} is the peak compressive strength, u_{cp} is the normal compressive displacement at peak compressive strength and u_{inel} is the inelastic normal compressive displacement.

The inelastic displacement is the irrecoverable displacement calculated as the total subcontact displacement (u_n^c) subtracted by the displacement at elastic compressive stress ($f_{c;el}$). The peak compressive displacement is formulated in Eq. (26). It is controlled by a non-dimensional parameter n, which is the factor of the supposed displacement at peak compressive strength under the initial stiffness.

$$u_{cp} = n \cdot \frac{f_{cp}}{k_n} \tag{26}$$

After the peak compressive strength is reached, compressive damage is initiated, and the compressive damage parameter d_c that controls the strength degradation under compression is calculated. The damage parameter is formulated in Eq. (27), referencing the implementation of the computational strategy proposed by Lourenço and Rots [27].

$$d_c = \begin{cases} 0, & u_n^c < u_{c,p} \\ \left(1 - \frac{f_{cm}}{f_{cp}}\right)\left(\frac{u_n^c - u_{cp}}{u_{cm} - u_{cp}}\right)^2 & u_{cp} \le u_n^c < u_{cm} \\ \left(1 - \frac{f_{cr}}{f_{cp}}\right) - \frac{f_{cm} - f_{cr}}{f_{cp}} \exp\left(\alpha \frac{u_n^c - u_{cm}}{f_{cm} - f_{cr}}\right) & u_n^c \ge u_{cm} \end{cases} \tag{27}$$

where f_{cm} is the intermediate compressive stress between peak and residual compressive strength, defined as the point of inflection from quadratic to exponential softening, f_{cr} is the residual compressive strength, u_{cm} is the displacement at intermediate compressive strength, and α is the parameter defining the slope of the exponential function, defined in Eq. (28).

$$\alpha = 2\frac{f_{cm} - f_{cp}}{u_{cm} - u_{cp}} \tag{28}$$

The intermediate compressive strength is fixed as the average value between peak and residual compressive strength. The compressive damage variable d_c is used to calculate the current compressive strength $\sigma_c(u_n^c)$ in Eq. (29).

$$\sigma_c(u_n^c) = (1 - d_c) \cdot f_{cp} \tag{29}$$

Intuitively, it can be seen from the last branch in Eq. (27) that the compressive damage variable d_c will asymptotically reach $\left(1 - \frac{f_{cr}}{f_{cp}}\right)$, which indicates that the masonry system will never be 'fully' damaged if there is a residual compressive strength. This differs from the implementation of linear softening, where the damage variable reaches 1.0 when the normal compressive strength exceeds the ultimate subcontact compressive displacement [58].

Similar to the displacement at peak compressive strength in Equation (26), the displacement at intermediate compressive strength is controlled by a non-dimensional parameter m as a factor to the displacement at peak compressive strength, as defined in Eq. (30).

$$u_{cm} = m \cdot u_{cp} \tag{30}$$

However, in contrast with the peak ratio, the non-dimensional parameter m is not a user-defined parameter. It is instead associated with the compressive fracture energy G_c as shown in Eq. (31).

$$m = \frac{G_c - 0.5\frac{f_{cp}^2}{9k_n} - 0.65(u_{cp} - u_{c;el})f_{cp} + 0.75\kappa + 0.25\xi}{\kappa + \xi} \tag{31}$$

where G_c is the compressive fracture energy, $u_{c;el}$ is the displacement at elastic compressive stress $f_{c;el}$, defined as $f_{c;el}/k_n$, κ and ξ are defined in Eq. (32).

$$\kappa = u_{cp}f_{cp} \quad \text{and} \quad \xi = u_{cp}f_{cr} \tag{32}$$

By associating m with the compressive fracture energy G_c, the predicted fracture energy under the hardening/softening law can be approximated to that calculated based on the multi-linear softening law. The minimum value of G_c is higher than the energy dissipated before the peak compressive strength is reached, ensuring that the m is larger than 1.

3.3. Force update routine

Within the context of an explicit time-marching integration scheme, the proper handling of force corrections upon damage is important to ensure the stability of the numerical simulations. This section explains the force update routine on each failure regime when the failure surfaces are violated.

The inadmissible contact stresses are mapped back to the yield surface upon violation of the pre-defined yield criterion. It is worth recalling that the yield value degrades as the relative subcontact displacement progresses on each regime. This behavior is defined in Eq. (33) for the tensile regime.

$$\text{If} \quad F_1 > 0, \quad \text{then} \quad F_n^t = f_t(u_n^t)A_c \quad \text{and} \quad \Delta F_n = 0 \tag{33}$$

Meanwhile, if F_2 in Eq. (14b) is violated, the subcontact shear force is corrected proportionally to the shear strength that also degrades as the shear displacement increases, defined in Eq. (34), where $|F_s|$ is the magnitude of the subcontact shear force vector.

$$\text{If} \quad F_2 > 0, \quad \text{then} \quad F_s := F_s\frac{f_s(u_s)A_c}{|F_s|} \quad \text{and} \quad \Delta F_s = 0 \tag{34}$$

Lastly, if F_3 is violated, the force is proportionally corrected by calculating the gradient vector to the point where the yield surface is violated and then reducing both normal and shear forces to the intercept of that gradient vector at the yield surface $F_3 = 0$. Once the intercept of the gradient vector at the yield surface is found, the correction procedure for normal and shear stresses is the same as that defined in Eqs. (33) and (34), respectively. The procedure is mathematically defined in Eq. (35) and illustrated in Fig. 8, where R_{trial} and R_{yield} are vectors for the violated force and the intercept at the yield surface towards the origin, respectively.

$$\text{If} \quad F_3 > 0, \quad \text{then} \quad F_n^c = \sigma^{yield}A_c \quad \text{and} \quad F_s := F_s\frac{\tau^{yield}A_c}{|F_s|} \tag{35}$$

Note that the yield surface will shrink due to strength degradation; hence, the force correction will always occur once the yield surface is violated unless the unloading occurs.

4. Material level validation of the contact model

Material characterization tests are often conducted to determine the material properties before a large-scale experimental test. The characterization tests are typically categorized into material tests on the masonry constituents (i.e., masonry units and mortar properties separately) and material tests on masonry as composite materials. It is important to note that within a block-based modeling strategy, the latter tests are required

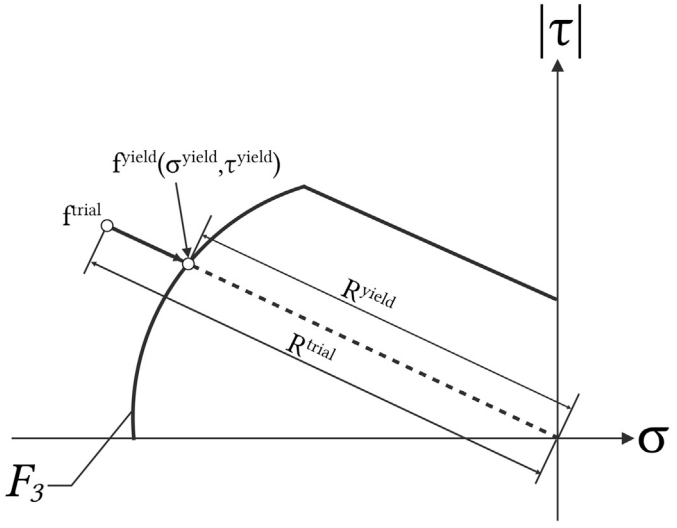

Fig. 8. Force update routine for the violation of yield surface F_3.

to calibrate and validate the input values assigned to the unit-mortar interfaces. In this section, a series of material characterization tests were selected to highlight the capability of the proposed model to simulate masonry failure in tension, shear, compression, and combined modes. For this scope, two distinct testing campaigns were selected, one conducted by van der Pluijm [64] on solid clay bricks and one by Esposito et al. [67] on solid calcium silicate (CS) bricks.

Since the experimentally obtained elastic properties are valid for the actual dimensions of the mortar joints and units, homogenization is required to relate the elastic properties of the extended unit with zero-thickness unit-mortar interfaces [68]. This can be done by assuming the same elastic properties between the extended and actual unit dimensions and that both configurations experience the same elongation. The normal and shear stiffnesses are then obtained as defined in Eq. (36) [68].

$$k_n = \frac{E_b E_m}{t_m(E_b - E_m)} \quad and \quad k_s = \frac{G_b G_m}{t_m(G_b - G_m)} \tag{36}$$

where E_b and E_m are the brick and mortar Young's Moduli, respectively, G_b and G_m are the brick and mortar shear moduli, respectively, and t_m is the thickness of the mortar joints.

The material properties used in the material level validation are given in Table 1. The material properties were obtained directly from the corresponding material tests: the van der Pluijm test [64] for the SC case and the experimental campaign by Esposito et al. [67] for the FPB, CV, and CH cases. Specifically, for the SC test, the mortar Young's Modulus was calibrated to reproduce the experimentally observed stress-displacement response.

The deformable block configuration is used for all simulations with the same mesh discretizations. The brick units are represented as linear elastic blocks with blown-up dimensions up to half of the mortar thickness. The mortar joints are not explicitly modeled and are modeled by zero-thickness interfaces where the deformation of the system is lumped. The dilatancy angle is set to zero in all models considered in this subsection.

The non-dimensional post-peak softening curve for tensile and shear are presented in Fig. 9. Since a series of tests conducted by various researchers [64,67,69–71] proved solid clay brick masonry to be more brittle compared to CS masonry, the damage profiles in tension and shear have to be defined differently. The tensile and shear damage profile for the solid clay bricks in the test conducted by van der Pluijm [64] is built using the exponential softening function by Lourenço and Rots [27] divided into 100 equal steps, presented as black solid lines in Fig. 9. The damage profile for CS masonry, given as dashed red lines in Fig. 9, is defined according to Esposito et al. [67].

Table 1
Material properties used in the validation case.

Material parameters	Unit	Value[a]			
		SC	FPB	CV	CH
Unit properties					
E_b	GPa	16.7		4.8	
ρ	kg m^{-3}	2300		1800	
$f_{s,b}$	MPa	-	3.1	3.0	
$f_{t,b}$	MPa	-	1.55	1.5	
ϕ_p	°	-		36.87	
Interface properties					
E_m	GPa	1.37[b]	1.2[b]	2.5	
k_n	GPa m^{-1}	150[c]	158[c]	521[c]	
k_s	GPa m^{-1}	70[c]	68[c]	227[c]	
f_{sp}	MPa	1.0	0.15	0.11	
f_t	MPa	0.3	0.11	0.1	
f_{cp}	MPa	-	-	5.93	7.55
G_c	N m^{-1}	-	-	31500	
f_{sr}	MPa	0.1		$0.1 f_{sp}$	
ϕ_p	°	45	29.64	23.27	
ϕ_r	°	35	28.37	23.27	

[a] SC: Shear-compression, FPB: Four-point bending, CV: Vertical compression, CH: Horizontal compression tests.
[b] Calibrated such that the global numerical response matched the experimental response.
[c] Derived values from Eq. (36).

4.1. Masonry couplet under combined shear-compression

The simplest material characterization test for masonry as a composite structure is the masonry couplet test. In the experimental test conducted by van der Pluijm [64], a masonry couplet was subjected to constant compressive load and a displacement-controlled lateral load. The test was performed on clay brick masonry couplets with unit dimensions of 210 mm × 80 mm × 100 mm (L × H × W) and the mortar joint thickness of 10 mm. Three different levels of pre-compression stresses were considered in this experiment: 0.1, 0.5, and 1.0 MPa.

In the numerical model, the nodes of the bottom block are fixed in all directions. The system is first brought to equilibrium under gravitational load, followed by applying the pre-compression stress at the top surface of the top block. Then, a lateral velocity of 2.5 mm s^{-1} is applied until the displacement reaches 3.0 mm. The comparison between numerical prediction with the implemented contact constitutive model and the experimental test is presented in Fig. 10. The contact model can predict the shear capacity and the post-peak behavior within the range of the upper bound and lower bound for all pre-compression levels.

4.2. Masonry wallets behavior under flexural load

Four-point bending tests are often conducted for quasi-brittle materials, such as concrete and masonry, to investigate the bending properties of masonry in terms of flexural strength and fracture energy in bending [72]. The four-point bending tests validated herein are taken from a series of tests conducted by Esposito et al. [67] for both calcium silicate and clay bricks. Only the calcium silicate specimens are considered for validation in this paper.

The four-point bending test setup is presented in Fig. 11. The bending properties are usually characterized by considering two configurations of four-point bending tests [73]; the test with the moment vector parallel to the bed joints (OOP-1 in Fig. 11a) and orthogonal to the bed joints (OOP-2 in Fig. 11b). An additional non-standardized four-point bending with the moment vector orthogonal to the plane of the wall (IP in Fig. 11c) is also considered to compare the masonry wallets' in-plane and out-of-plane vertical flexural strength.

The wall specimen comprises 2 × 10 courses of 210 × 70 × 100 mm^3 (L × H × W) calcium silicate bricks for the OOP1 test, while the OOP2 and IP tests comprise 4 × 4 courses of bricks. The distance between the loading points was set at 360 mm, and the distance between the roller supports was set at 720 mm.

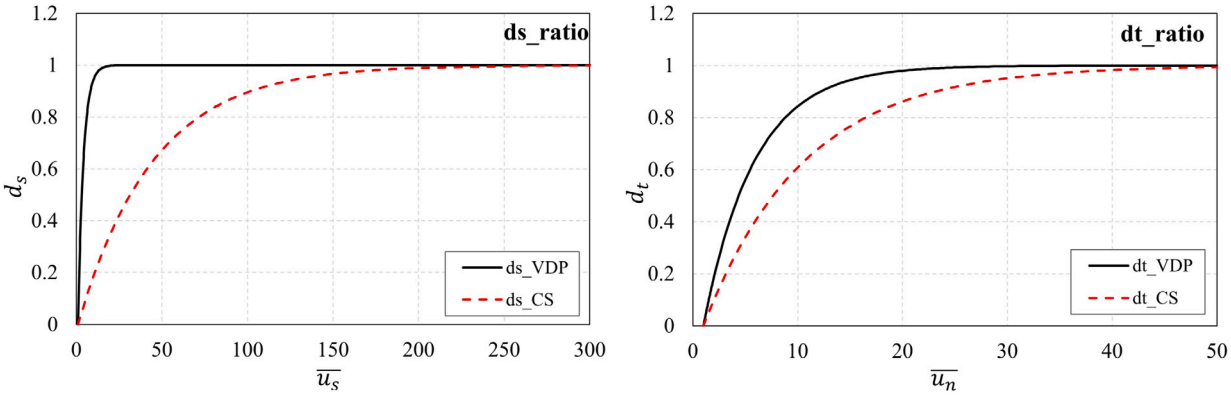

(a) d_s ratio (b) d_t ratio

Fig. 9. Shear and tensile post-peak softening behaviors for the couplet test. VDP: van der Pluijm test campaign [64], CS: testing campaign on CS masonry [67].

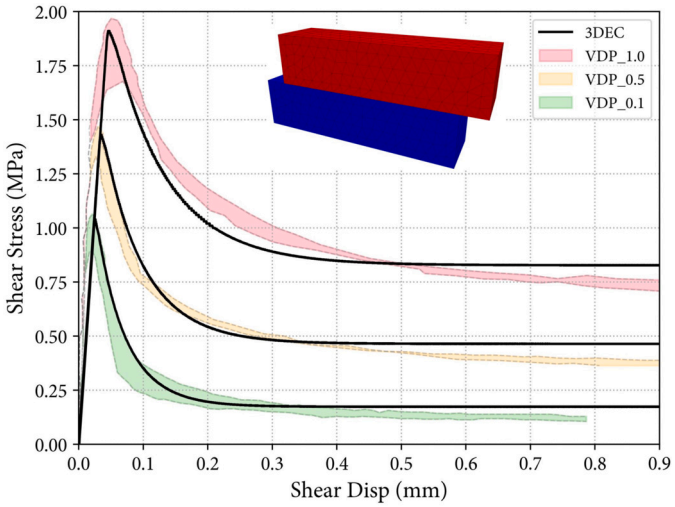

Fig. 10. Comparison of experimental and numerical responses of the couplet test [64].

The model configuration for the four-point bending tests is shown in Fig. 12. The displacement-controlled load is applied as line load for OOP1 and OOP2, as shown in Figs. 12a and 12b, respectively. In order to conduct the IP test (Fig. 12c), it is necessary to ensure that the loading plate remains orthogonal to the plane of the masonry wall. Therefore, the load is applied through a plate modeled via rigid blocks. Similarly, for the boundary conditions, the roller supports are directly applied to the nodal points in the OOP1 and OOP2 models, while the supports for the IP model are defined through rigid blocks representing the steel roller supports in the experiment. The linear elastic law is applied to the contact points between the masonry blocks and the loading and support plates.

The material properties for the four-point bending tests are presented in Table 1. The same properties are applied to all tests to maintain consistency. The displacement in the experiment is obtained from linear interpolation of the vertical Linear Variable Differential Transformers (LVDTs), while the displacement in the numerical simulation is obtained by averaging the nodal points in the mid-span of each model. The force in the numerical simulation is tracked by defining a subroutine in the *3DEC* software, based on the FISH function, an executable programming language by ITASCA.

The force-displacement curves of all four-point bending tests are presented in Fig. 13. The material characterization tests were run 6 times for each configuration for statistical purposes. Readers are referred to the report by Esposito et al. [67] for the full details on each test result. The numerical model was able to predict the global behavior of the experimental specimens relatively well despite using the same set of material properties for each test.

The numerical post-peak response for the IP case was also in good agreement with the experimentally observed behavior. The stable post-peak response for the IP case was due to the interlocking mechanism of the masonry units at the onset of failure, which provided stability to the specimens before full collapse was observed. On the other hand, the experimental post-peak response for the OOP1 and OOP2 cases cannot be compared as the tests were conducted so that the gravity effect was not retained at the onset of damage. This caused the immediate collapse of the experimental specimens soon after the peak load was achieved, as shown by the interruption of the experimental curves in Figs. 13a and 13b.

It is also clear from the force-displacement curve in Fig. 13 that the same experimental tests conducted multiple times would produce a scattered global response. To demonstrate the effect of material variability when compared against a deterministic numerical model, a comparison is drawn between the experimentally observed crack pattern and the numerically predicted deformed shape, presented in Fig. 14. The experimental photos in Figs. 14a and 14b correspond to the upper- and lower-bound results for the in-plane bending force-displacement tests shown in Fig. 13c, respectively. The experimental crack pattern exhibited the same crack initiation (from the bottom-most section of the mid-span) but different crack propagation for the same loading protocols and materials from the same batch, i.e., supposedly the same material properties. The crack found in the upper-bound test (Fig. 14a) propagated to the left side of the mid-span region while the lower-bound (Fig. 14b) propagated to the right.

The numerical model predicted the crack initiation at the bottom-most section of the mid-span region in Fig. 14c. However, in contrast with the experimentally observed crack pattern, the crack propagation was symmetric and localized only in the mid-span region of the model. Such different crack propagation within the same material properties and loading protocols could be attributed to the spatial variability of the material properties, as reported by several researchers [74–76]. Nevertheless, despite the material variability observed in the experimental specimens, the numerical model could still predict the peak load and stiffness, as well as the post-peak behavior in some cases, in a relatively accurate manner.

4.3. Masonry prism subjected to pure compressive load

The performance of the contact constitutive model under monotonic uniaxial compressive loading is validated using the same series of experiments conducted by Esposito et al. [67] on calcium silicate bricks. The compression test is conducted in accordance with the standard EN

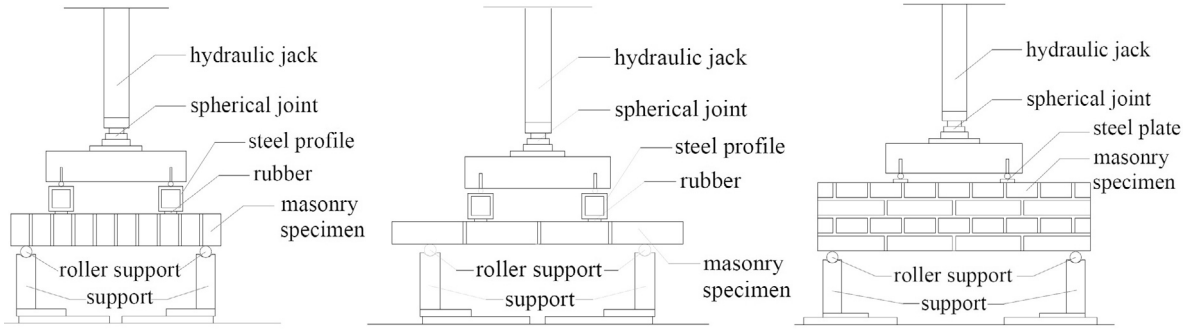

(a) OOP-1 (b) OOP-2 (c) IP

Fig. 11. Experimental set-ups for the four-point bending tests [67].

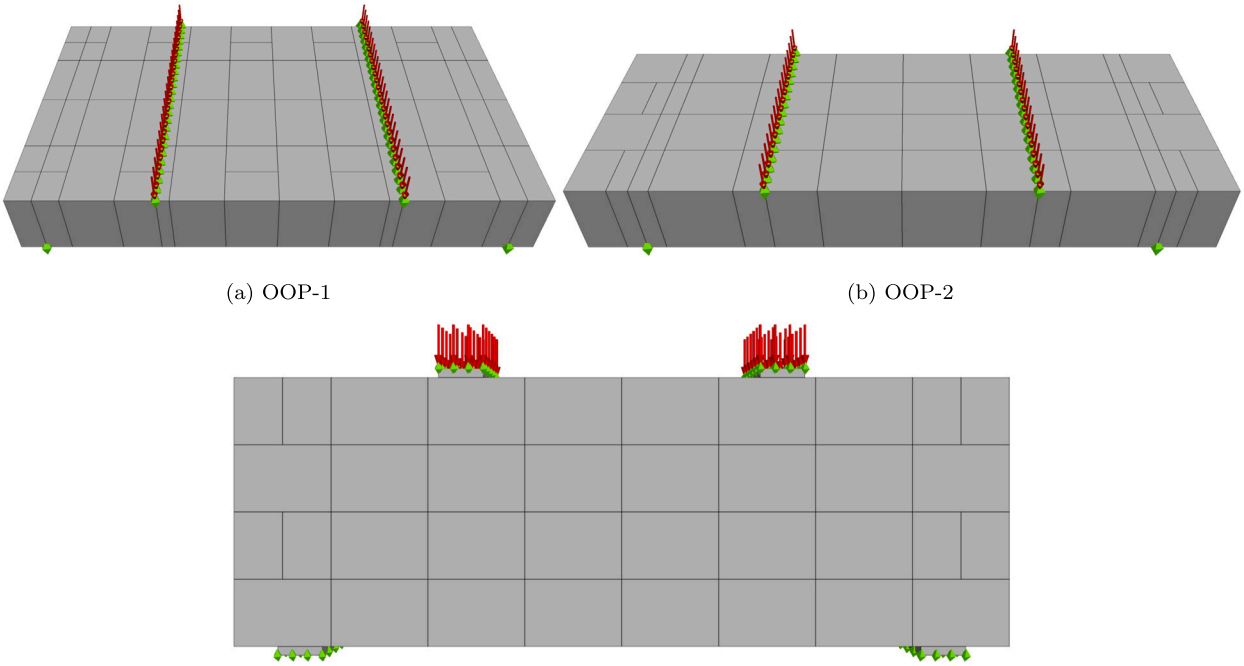

(a) OOP-1 (b) OOP-2

(c) IP

Fig. 12. Model setup for the four-point bending tests in 3DEC [48].

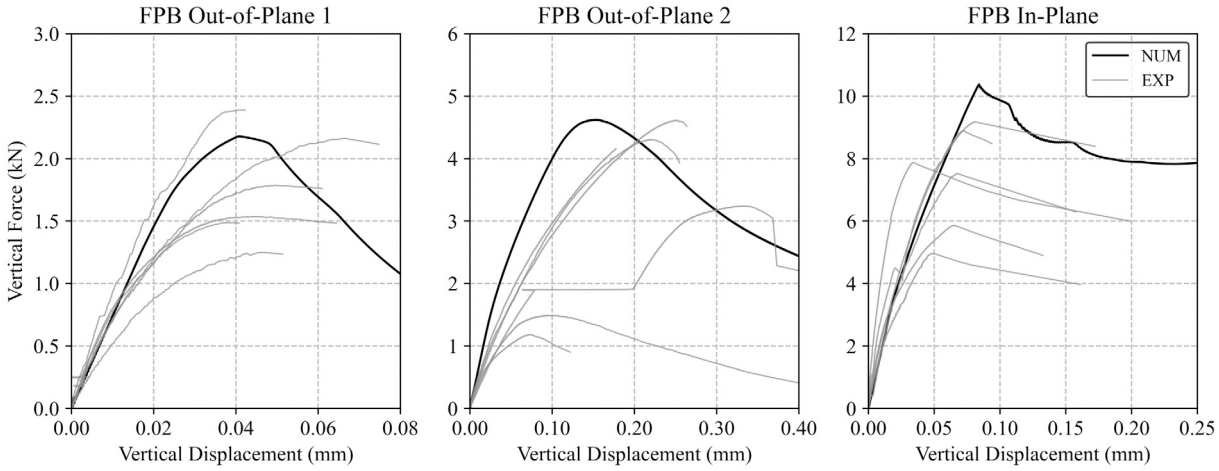

(a) OOP-1 (b) OOP-2 (c) IP

Fig. 13. Force-displacement comparison of the four-point bending tests.

(a) TUD EXP MAT14b (b) TUD EXP MAT14a

(c) NUM FPB IP (Def. factor:100)

Fig. 14. Comparison of (a), (b) experimental crack pattern and (c) numerical deformed shape (magnified 100 times).

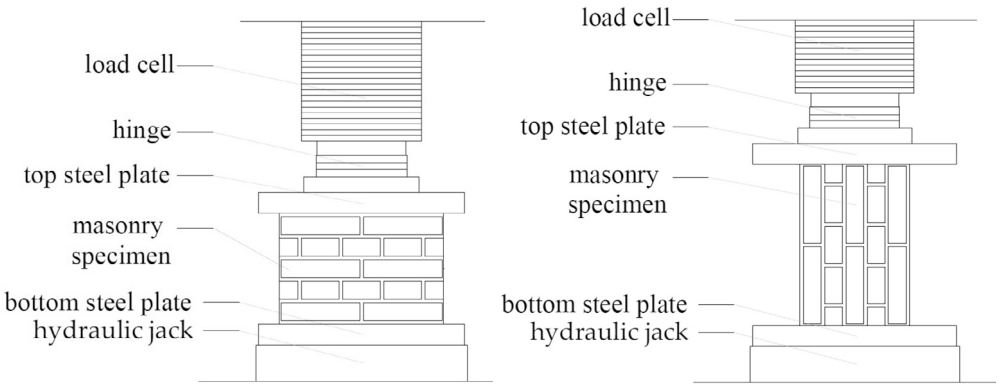

(a) Vertical configuration (b) Horizontal configuration

Fig. 15. Compressive test setup on masonry prism [67].

1052-1:1998. The masonry prism comprises 2 × 6 courses (L × H) of brick units with a 10 mm layer of mortar joints.

The experimental setup is presented in Fig. 15. There are two configurations considered in the test: a "vertical" configuration (Fig. 15a) where the load was perpendicular to the bed joints, which is in line with the European standard, and a "horizontal" configuration (Fig. 15b) where the compression load was parallel to the bed joints. The latter was used to observe the orthotropic behavior of the masonry prism. The numerical modeling for this test is straightforward, where the displacement-controlled compressive load is applied at the bottom of the model through a rigid loading plate with the support located at the top.

The material properties considered for this test are presented in Table 1. The peak ratio n is set at 68.5 and 85 for the vertical and horizontal tests, respectively. The reason for such a high peak ratio is due to the fact that calcium silicate masonry wallets often exhibit a higher secant elastic modulus, evaluated at 30% of the compressive strength, compared to clay bricks, but the responses are followed by a longer hardening before the peak compressive strength is reached compared to those of clay masonry wallets [67,72].

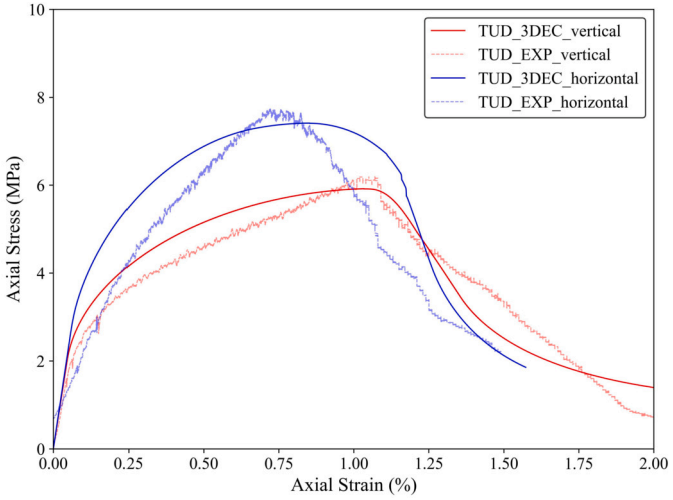

Fig. 16. Stress-strain comparison of the direct compression test.

The axial strain recorded in the pre-peak phase was taken from the displacements recorded in the set of LVDTs attached to the specimen. However, since rotation and detachment of the LVDTs caused by the large post-peak deformations were observed in the experiment, the post-peak displacement readings from the LVDTs were disregarded. Instead, the readings from the hydraulic loading jack were used to obtain the stress-strain relationship. Similarly, the pre-peak strain recorded in the numerical model was taken from the displacement at the measurement locations of the LVDTs, while the post-peak strain was taken from the displacement at the loading plate.

The comparison of the stress-strain diagram between the numerical model and the averaged result from the series of compression tests for each configuration is presented in Fig. 16. It is evident that the predicted peak compressive strengths are in good agreement with the experimentally observed responses. However, the hardening and softening curves for each test configuration could still be improved by calibrating the peak ratio parameter according to the averaged experimental responses.

In conclusion, the material-level validations showed that the proposed contact constitutive model offers sufficient accuracy and capability to capture associated failure mechanisms. In the next section, the contact constitutive model will be validated on a larger scale with complex failure mechanisms.

5. Structural level validation of masonry walls under in-plane loading using DEM

In this section, the contact constitutive model is validated against a series of unreinforced masonry (URM) wall experiments that captured a complex failure mechanism with combined flexural and diagonal cracks both along the mortar joints and through the bricks, including crushing of compressed toes. The widely referred masonry wall experiment by Vermeltfoort et al. [77] is used to validate the implemented contact constitutive model. While two wall configurations (complete wall panels without opening and wall panels with opening in the center) were tested in the experiment, this paper simulates only complete wall panels without openings. The experimental study reported a series of experiments on masonry walls with dimensions of 0.99 × 1.00 mm^2 subjected to restrained vertical deformations with displacement-controlled monotonically increasing lateral loading. The wall experiments were preloaded with vertical compression stress (σ_v) of 0.3 MPa, 1.21 MPa, and 2.1 MPa, termed in this paper as “LOW”, “MID”, and “HIGH” compression wall specimens, respectively.

Table 2
Material properties as input parameters to the numerical model.

Masonry unit properties					
E_b, υ	$k_{n,b}$, $k_{s,b}$	$f_{t,b}$	$f_{sp,b}$, $f_{sr,b}$	$\phi_{p,b}$	ρ
(GPa,[-])	(GPa m^{-1})	(MPa)	(MPa)	(°)	(kg m^{-3})
16.7, 0.15	820, 360	2.0	2.8, 0.0	45	1800
Interface properties - σ_v = 0.30 MPa					
k_n, k_s	f_t, f_{cp}	f_{sp}, f_{sr}	ϕ_p, ϕ_r	G_c, n	C_n, C_{nn}, C_{ss}
(GPa m^{-1})	(MPa)	(MPa)	(°)	(N m^{-1},[-])	([-])
82, 36	0.25, 10.5	0.35, 0.0	35, 35	5000, 2.0	0.0, 1.0, 9.0
Interface properties - σ_v = 1.21 MPa					
k_n, k_s	f_t, f_{cp}	f_{sp}, f_{sr}	ϕ_p, ϕ_r	G_c, n	C_n, C_{nn}, C_{ss}
(GPa m^{-1})	(MPa)	(MPa)	(°)	(N m^{-1},[-])	([-])
110, 50	0.16, 11.5	0.22, 0.0	35, 35	5000, 2.0	0.0, 1.0, 9.0
Interface properties - σ_v = 2.12 MPa					
k_n, k_s	f_t, f_{cp}	f_{sp}, f_{sr}	ϕ_p, ϕ_r	G_c, n	C_n, C_{nn}, C_{ss}
(GPa m^{-1})	(MPa)	(MPa)	(°)	(N m^{-1},[-])	([-])
82, 36	0.16, 11.5	0.22, 0.0	35, 35	5000, 2.0	0.0, 1.0, 9.0

5.1. Experimental and numerical setups

The masonry wall specimen comprised 18 courses of solid clay bricks with dimensions of 204 × 98 × 50 mm^3 (L × W × H). The bottom- and top-most courses were clamped to the steel beams, in which a vertical compression load and a monotonic displacement-controlled lateral load were applied to the top steel beam. The experimentally observed damage pattern at the end of the analysis for both tested vertical stresses is shown in Fig. 17. At both tests, horizontal flexural cracks initially formed at the bottom- and top-most part of the wall specimen. Diagonal shear cracks were then observed, followed by a gradual drop in lateral capacity. The reported failure of all tested walls was due to the formation of diagonal cracks and crushing observed at the toes of the wall specimens.

It is evident from the crack pattern that the diagonal cracks on the LOW compression model (Fig. 17a) were more localized, with a few cracks through the brick units. As the pre-compression load increased to the MID compression model (Fig. 17b), the cracks through the bricks became apparent. Finally, the diagonal cracks on the HIGH compression model (Fig. 17c) were more dispersed, with comparatively more cracks through the brick units.

The model geometry and the corresponding joint plane discretization are presented in Figs. 18a and 18b, respectively. The masonry unit is discretized as two deformable blocks joined by a potential crack surface at half-length of the brick unit. The bond (unit-mortar interface) is defined at the mortar joint locations. Two rigid blocks representing the support and loading plates are modeled and connected to the masonry specimen through linear elastic contact planes (orange-colored surfaces in Fig. 18b).

Similar to the experiment, a double-clamped boundary condition is applied to the model where only the lateral direction of the top block is freed. The vertical displacement of the top block is freed when the axial stress is applied and fixed when the lateral displacement-controlled load is applied. The material properties of the contact points are taken from the main literature as well as references from various researchers that used the experimental results as validation cases [27,29,30,32,33,47,78]. The input parameters are summarized in Table 2 for each pre-compression level.

The peak ratio n is taken as 2.0 considering the recommendation from the material characterization test on solid clay bricks conducted by Jafari [79]. Since there were no material characterization tests given in this original experiment, the softening curve is obtained using the equation for exponential softening in tension and shear defined by Lourenço and Rots [27] divided into 200 linear segments. The post-peak softening behaviors in shear and tensile regimes are presented in Figs. 19a and 19b, respectively.

The system is first brought to equilibrium under gravity load, which is then followed by the application of the pre-compression load as distributed loads at the top surface of the upper rigid block. Once the

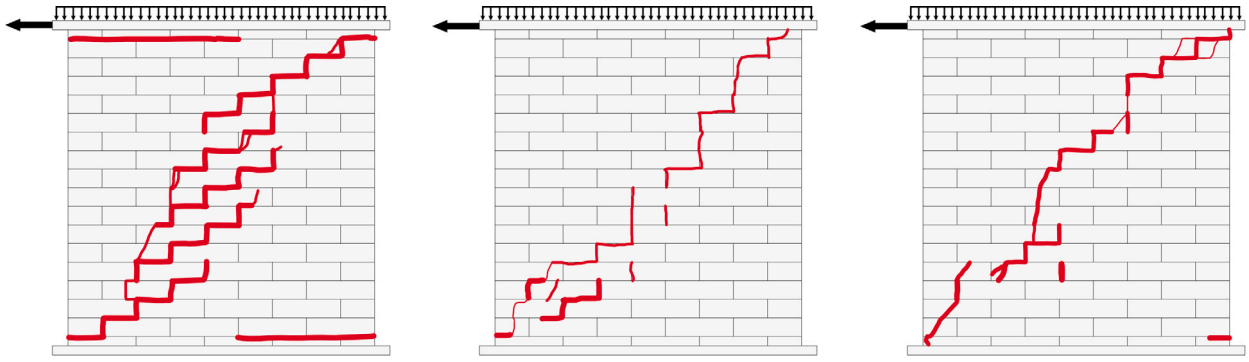

(a) σ_v: 0.30 MPa (LOW) (b) σ_v: 1.21 MPa (MID) (c) σ_v: 2.12 MPa (HIGH)

Fig. 17. Damage pattern of the shear-compression masonry wall test [77].

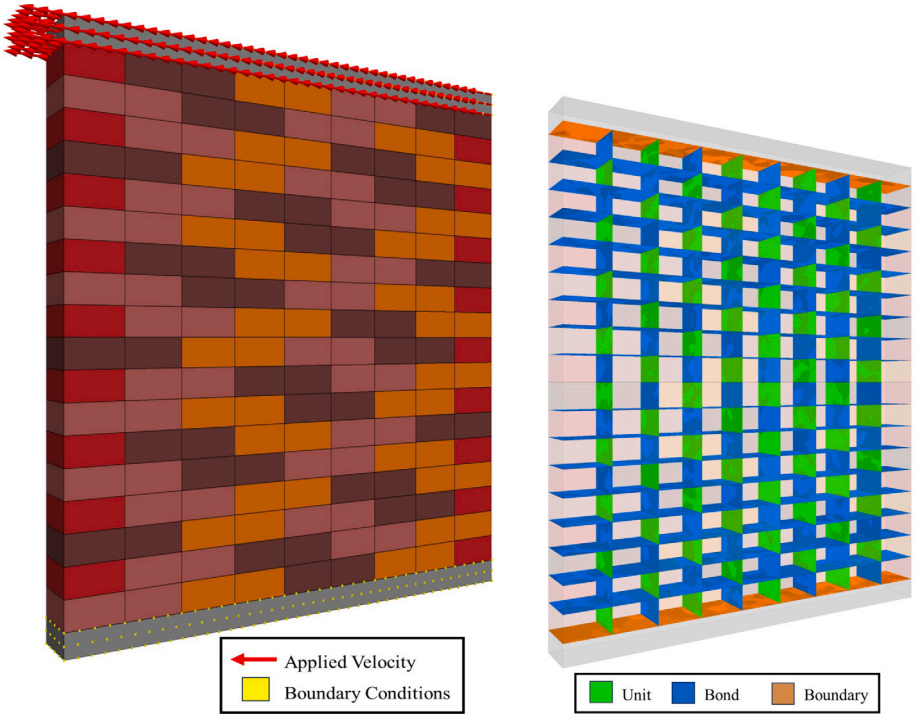

(a) Model geometry (b) Joint geometry

Fig. 18. Brick discretization of the solid URM wall experiment.

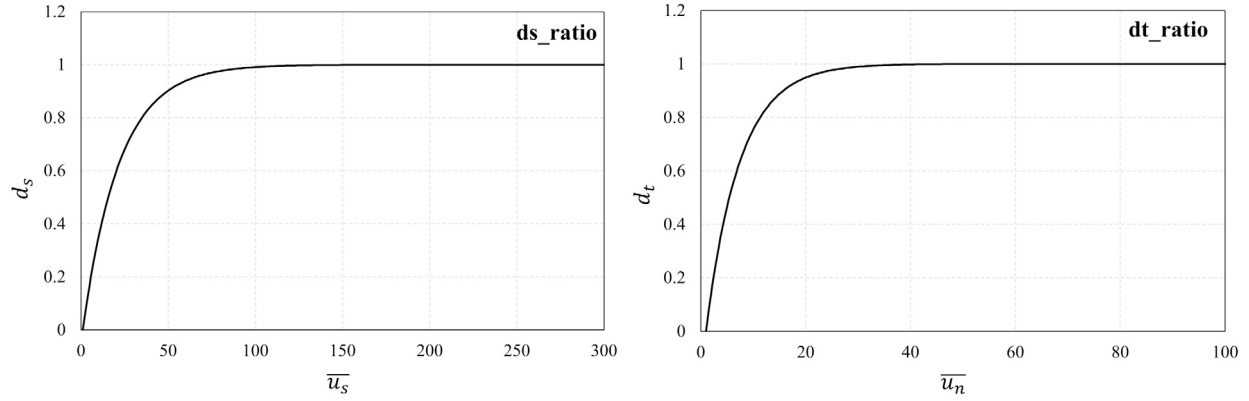

(a) d_s ratio (b) d_t ratio

Fig. 19. Shear and tensile post-peak softening behaviors for the monotonic shear-compression wall test.

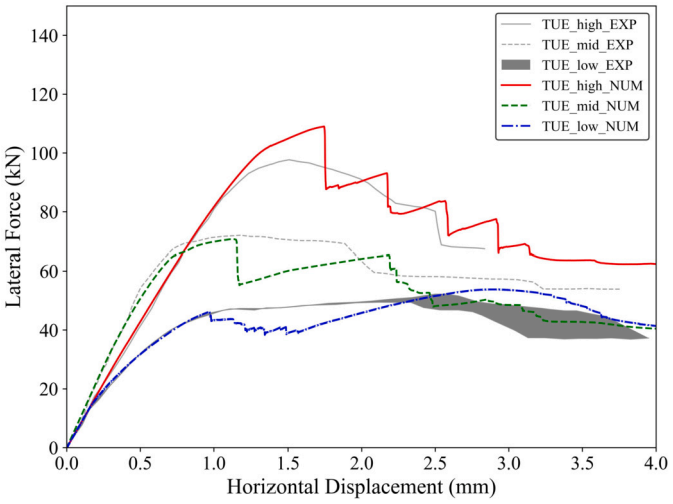

Fig. 20. Force-displacement response comparison at each pre-compression level.

equilibrium is achieved again, the top block vertical displacement is fixed, and the lateral load is applied as a velocity with a constant rate of 1 mm s^{-1}.

5.2. Validation results and discussions

A comparison of force-displacement response between the numerical models (indicated as "NUM") and the experimental findings (indicated as "EXP") at each precompression level is presented in Fig. 20. The wall experiment with low pre-compression stress was conducted twice, hence the bounded force-displacement curve. The numerical model was capable of predicting the global behavior of the experimental specimens with relatively good accuracy.

For the wall model with the LOW pre-compression level (σ_v = 0.30 MPa), the blue line in Fig. 20, the experimental force-displacement curve was relatively 'ductile' with a stable response up to the horizontal displacement of 2.5 mm and a gradual loss of load-carrying capacity afterward. The numerical model for the low pre-compression stress exhibited a brief decline in shear capacity as the lateral displacement reached 1.0 mm. This drop is caused by the sudden opening of the diagonal crack through the mortar joints and the potential crack surface at the brick units [80], as presented by the evolution of the combined shear-tension damage parameter d_{ts} plot in Fig. 21. The diagonal crack was fully formed as the lateral displacement reached 2.0 mm. Since no compressive damage was observed when the diagonal crack formed, the model could regain its shear capacity as the displacement progressed to 3.0 mm when toe crushing was observed, and the capacity dropped gradually afterward.

Similarly, for the MID model (σ_v = 1.21 MPa), the green line in Fig. 20, the experimental force-displacement curve was stable up to the lateral displacement of 1.0 mm, where the opening of the unit-mortar interfaces occurred at the diagonal strut. In contrast with the LOW model, the MID model experienced more cracks through the potential crack surfaces, which caused the sharp decline in load capacity as the lateral displacement progressed to 2.0 mm. Although cracks through the brick units are more apparent in the MID model, the diagonal crack was still localized in one single strut, as shown in the combined shear-tensile damage variable plot in Fig. 21.

The wall model under high pre-compression stress (σ_v = 2.12 MPa) resisted a higher peak load capacity of approximately 100 kN (the red line in Fig. 20), which was followed by a rapid degradation of the shear capacity due to the opening of the diagonal crack not only along the mortar joints but also through the bricks. During the splitting of the brick units, there is a transfer of subcontact forces to the adjacent units as they push toward each other. The transference of subcontact forces leads to the increase of frictional resistance at the adjacent blocks, resulting in the regain of capacity after the shear capacity drops in Fig. 20. The increase in frictional resistance takes place until another splitting through the brick occurs, causing another drop in the shear capacity. This behavior persisted until crushing at the compressed toes took place beyond the lateral displacement of 3.5 mm.

The damage progression and formation of the diagonal cracks for the high pre-compression model are also well-represented by the tension-shear damage parameter d_{ts} plot in Fig. 21, where the diagonal cracks formed between 1.0 mm and 2.0 mm, which included both the openings of the mortar joints and the potential crack surfaces on the brick units and progressed until the full formation of the diagonal cracks at the horizontal displacement of 3.0 mm.

Unlike the behavior observed during the experiment, where inclined cracks could occur through the units, the cracks in the numerical model were 'forced' to happen in the middle of the brick units through the potential crack surfaces, which caused the stepwise numerical force-displacement curve in contrast with the smooth decline of the experimental force-displacement curve in Fig. 20. This stepwise behavior persisted until the crushing damage at the compressed toes was observed at the horizontal displacement of 3.0 mm. An alternative solution to alleviate this behavior is to refine the potential crack surfaces into multiple planes, resulting in smoother crack representations on the brick units.

The crack pattern at the end of the analysis (at the horizontal displacement of 4.0 mm) at each pre-compression level is shown in Fig. 22, magnified 50 times. The collapse mechanisms are consistent with those observed during the experiments (Fig. 17). It is also evident that contact interpenetration between blocks was observed at the compressed toes within the diagonal cracks of the models in Fig. 22, indicating that compressive crushing occurred and localized within those regions.

5.3. Discussion on the numerical stability

The numerical stability in an explicit-based numerical method is quantified through the equilibrium error over the simulation. In this paper, the equilibrium error is defined as the ratio of out-of-balance force components that remain after the summation of the forces and the total forces being applied to the nodes. This is termed the local force ratio and is defined in Eq. (37) for a single node.

$$R = \frac{\langle \Sigma_i F_i^{OOB} \rangle}{\Sigma_i \langle F_i \rangle} \tag{37}$$

where R is the local force ratio on a single node, F_i^{OOB} is the out-of-balance force after the summation of forces that tends to zero upon equilibrium, and F_i is the total force (Eq. (9)). The $\langle \cdot \rangle$ sign indicates the sum of the absolute values of the vector components.

The plot of the maximum local force ratio of any nodes against the applied displacement for each case is presented in Fig. 23. Since the geometry and mesh sizes used across all three models are identical, the timestep for all models was also identical at 1.68×10^{-6} s. The LOW model exhibited significant fluctuations from 1.0 mm to 1.5 mm (Fig. 23a), which corresponded with the loss of shear capacity due to the opening of the diagonal cracks (Fig. 21 for the LOW model). The wall model experienced another series of fluctuations from 2.0 mm to 4.0 mm as more cracks were observed along the diagonal strut, followed by toe crushing.

On the other hand, the equilibrium error plot for the MID model (Fig. 23b) showed a relatively different behavior compared to the LOW model. The lesser fluctuations could be correlated with more occurrences of unit splitting in the MID model and better transference of the subcontact forces from the diagonal strut to the adjacent units. A slight increase in the equilibrium error occurred between 1.0 mm and 1.5 mm, and between 2.0 mm and 2.5 mm. These corresponded with the capacity loss due to the units splitting (Fig. 20).

The equilibrium error for the HIGH model showed a similar response to the other two models. The sharp increase in the equilibrium error

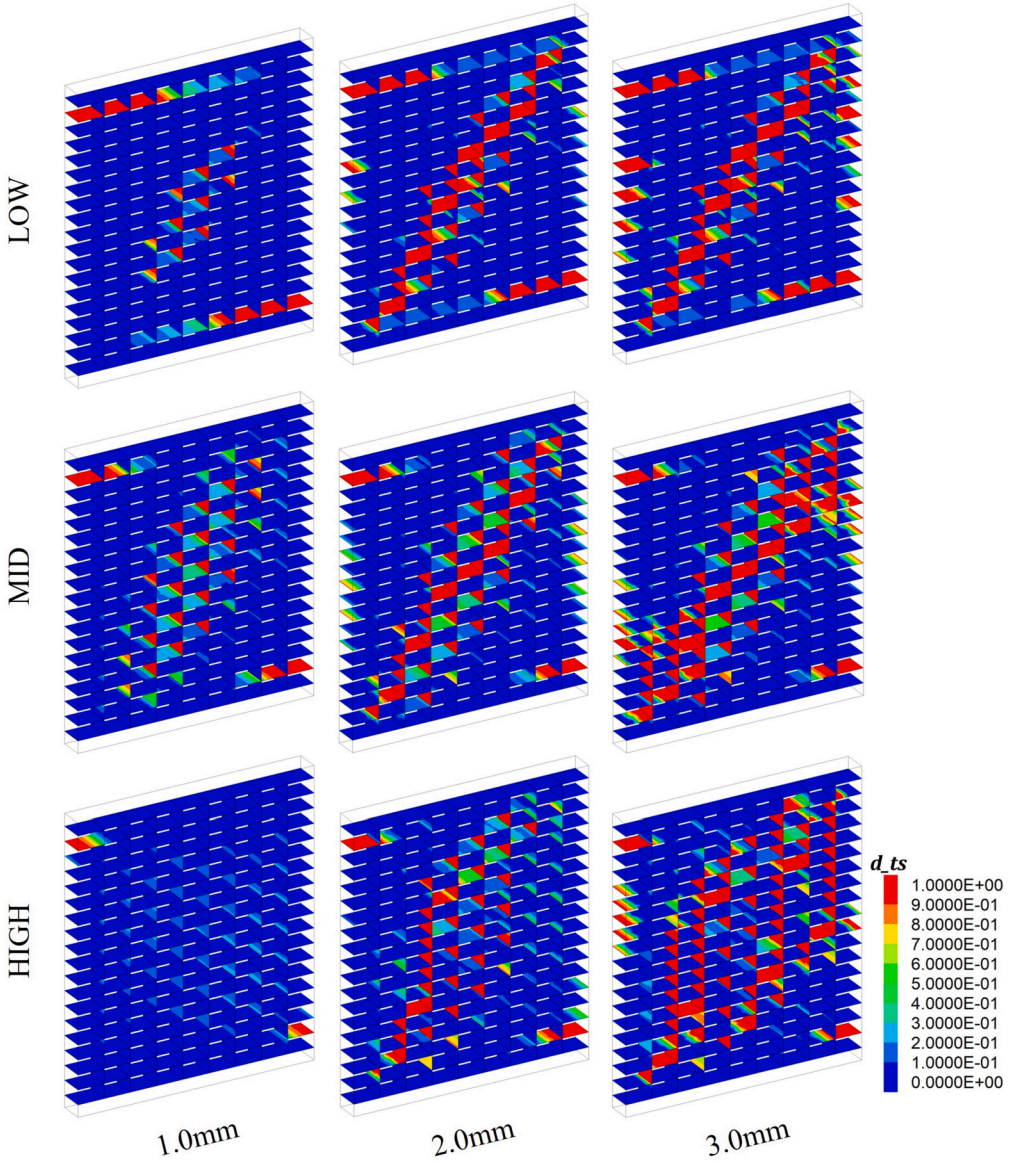

Fig. 21. Damage progression in combined tension and shear (d_{ts}) when lateral displacement is 1.0 mm,2.0 mm, and 3.0 mm (left to right).

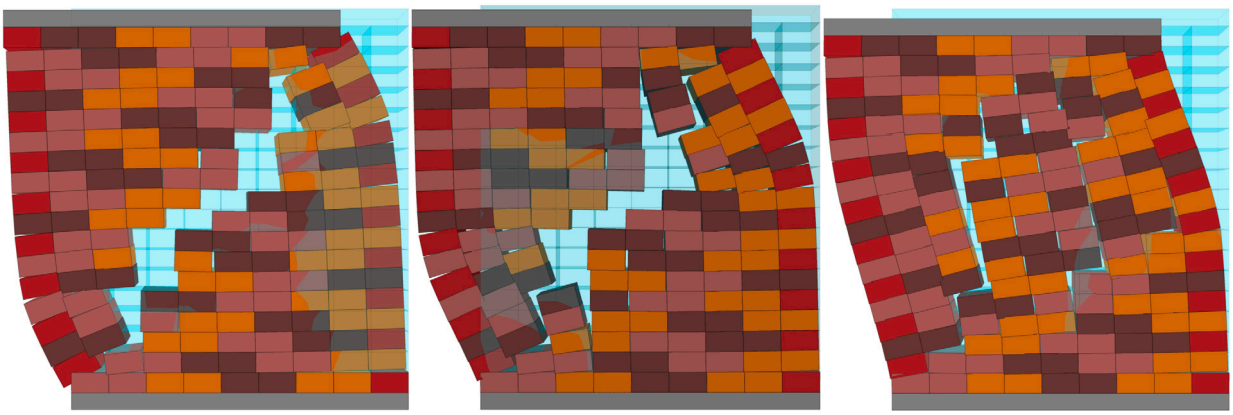

(a) LOW (b) MID (c) HIGH

Fig. 22. Crack pattern of the model at the end of the analysis (Def factor: 50).

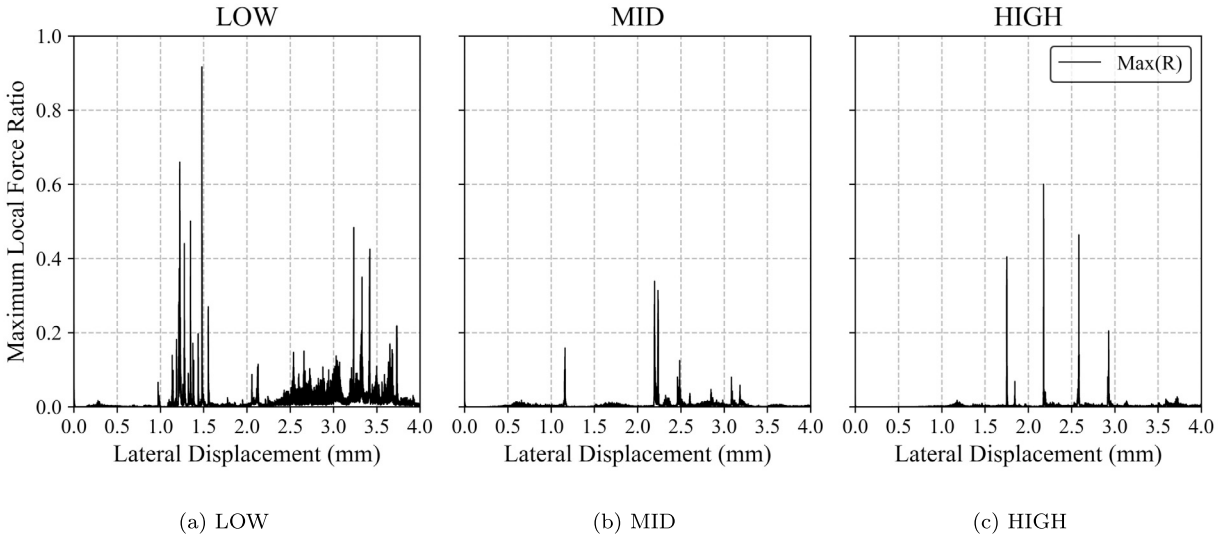

Fig. 23. Plot of maximum local force ratio vs applied displacement.

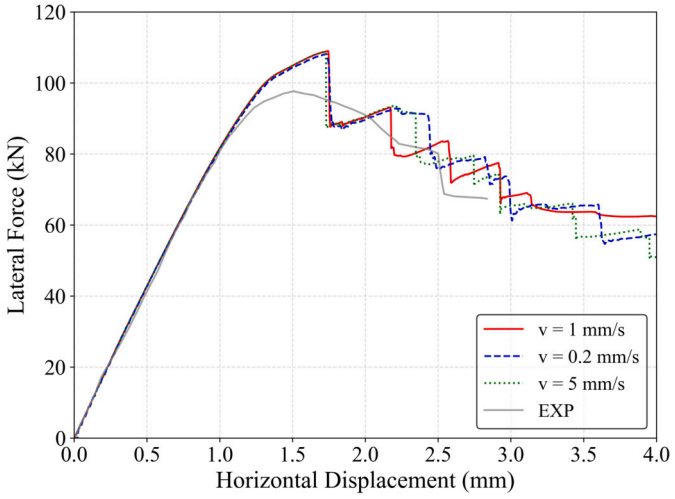

Fig. 24. Force-displacement curve of the HIGH model with different applied velocities.

due to the unit splitting was more distinct in the HIGH model, as shown in Fig. 23c where three peaks were observed from 1.7 mm to 2.6 mm which corresponded with the sudden drop in shear capacity as seen in Fig. 20. The HIGH model experienced another peak due to toe crushing at 2.9 mm.

5.4. Sensitivity analysis on the applied loading velocity

In this section, the sensitivity of the wall model to the applied loading velocity is compared. Using the HIGH wall model, the initial applied velocity of 1 mm s^{-1} is decreased to one-fifth of its value (0.2 mm s^{-1}) and increased to five times the original value (5 mm s^{-1}). The initial applied velocity was determined heuristically by monitoring the changes in the global response of the wall structure due to the inertial effect.

The force-displacement comparison of the HIGH model with different applied velocities is presented in Fig. 24. The peak load, corresponding displacement, and dissipated energy are quantified in Table 3. Compared to the benchmark model, where the simulation was finished in 27 hours, the simulation for the one-fifth model required 150 hours, while it took 5.4 hours to run the model with the applied velocity five times the original value.

Table 3
Quantification of the global responses for the HIGH model with different applied velocities.

Model Name	Peak load kN (%)[a]	Peak disp. mm (%)[a]	Diss. energy kN/mm (%)[a]
EXP	97.69	1.51	199.9
v = 1 mm s^{-1}	109.1 (-11.58)	1.74 (-15.62)	206.8[b] (-3.47)
v = 0.2 mm s^{-1}	108.16 (-10.71)	1.73 (-14.85)	209.4[b] (-4.74)
v = 5 mm s^{-1}	108.85 (-11.42)	1.73 (-14.65)	208.4[b] (4.28)

[a] Values in brackets represent the relative error percentage to experimental values.
[b] Dissipated energy calculated until the displacement at the end of the experiment.

From both Fig. 24 and Table 3, both the peak load and the corresponding displacement are almost identical, despite slight differences observed in the post-peak response. However, it is worth noting that the wall model may become more sensitive if the applied velocity is extremely increased such that the inertial effect can no longer be dampened by the local damping scheme in Eq. (11).

5.5. Discussion on the computational efficiency

This section discusses the computational efficiency of the DEM framework when combined with the proposed contact model. The research's numerical simulations were conducted on a Windows workstation equipped with a 2.6 GHz Intel Core i9 Processor and 32 GB of memory. The simulations of the low and high compression models reached a lateral displacement of 4.0 mm within 27 hours, with a constant lateral velocity of 1.0 mm s^{-1} and a local damping coefficient of 0.8. Additionally, both numerical simulations were executed consecutively, allowing the observation of the progressive failure of the masonry wall models without interruptions due to numerical instabilities commonly seen in implicit solution-based simulations [81]. The explicit-based DEM framework coupled with a suitable contact model for masonry structures is more robust in terms of numerical stability compared to implicit-based finite element simulations. However, the DEM framework requires smaller time steps for stability, leading to longer computational time.

To further highlight both the efficiency and accuracy of the proposed model, numerical simulation on the HIGH model is conducted using the Mohr-Coulomb (MC) contact model readily available in *3DEC* (Fig. 4).

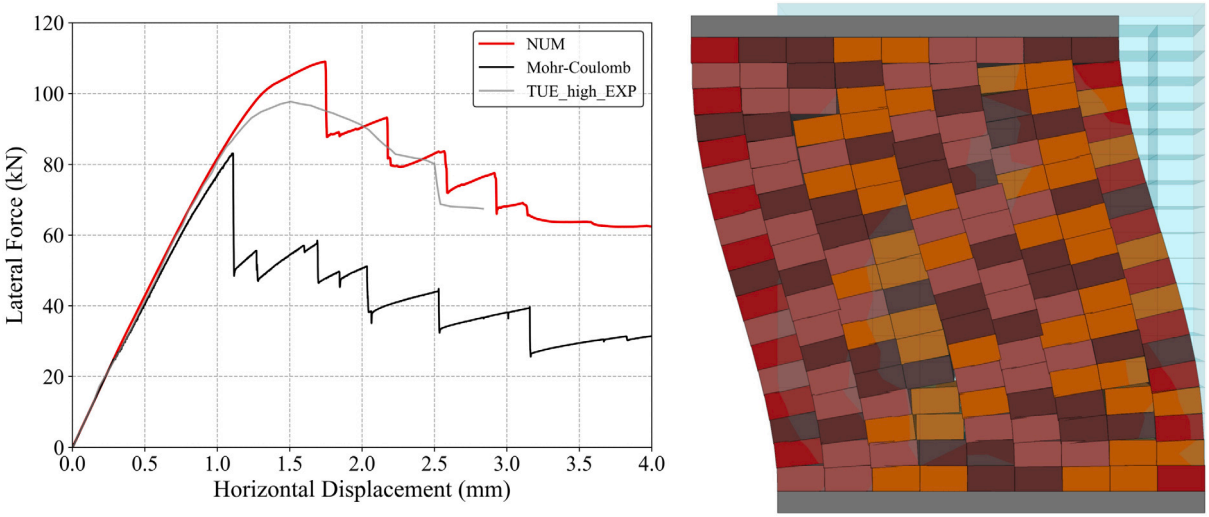

(a) Force-displacement curve (b) Deformed shape (Def Factor: 50)

Fig. 25. Numerical results of the high pre-compression wall test using Mohr-Coulomb (MC) model.

Table 4
Comparison of the proposed model to the Mohr-Coulomb contact model.

Model Name	Peak load kN (%)[a]	Peak disp. mm (%)[a]	Diss. energy kN/mm (%)[a]
Proposed model	109.1 (-11.58)	1.74 (-15.62)	206.8[b] (-3.47)
Mohr-Coulomb	83.12 (-14.92)	1.11 (-26.45)	128.07[b] (-35.95)

[a] Values in brackets represent the relative error percentage to experimental values.
[b] Dissipated energy calculated until the displacement at the end of the experiment.

The MC model is the standard contact constitutive model typically used in DEM for the numerical analysis of masonry structures, as it provides a brittle representation of damage in masonry constituents. The material elastic properties used in this simulation are taken from Table 2, along with the tensile strength (f_t), peak and residual cohesive strengths (f_{sp} and f_{sr}, respectively), and the peak and residual friction angle (ϕ_p and ϕ_r, respectively).

The force-displacement curve and the deformed shape of the wall model are presented in Fig. 25. The numerical simulation reached the 4.0 mm displacement within 29 hours using the same workstation as the proposed model. The computational time is comparable to the proposed model, further highlighting the negligible impact of adding hardening/softening and compressive cap functionalities to the contact constitutive model in DEM.

In terms of prediction accuracy of the global behavior (the force-displacement curve in Fig. 25a), the MC model provides significantly less accurate predictions than the proposed contact model. The sudden decline of shear capacity for the MC model was consistent with the straight cracks through the potential crack surfaces and unit-mortar interfaces, as depicted in the deformed shape in Fig. 25b. With more occurrences of slidings and separations of the interfaces in the MC model, the transference of subcontact forces to the adjacent subcontacts happened more frequently, leading to more sudden increases and decreases of the shear capacity in Fig. 25a.

The relative errors of the peak load and corresponding displacement and dissipated energy of the MC model are compared to the proposed contact model in Table 4. It is clear that although the peak load is within the margin of error of 20%, the corresponding displacement, dissipated energy, and the failure modes represented by the deformed shape are considerably different when compared to the experimental responses. Due to the inadequacy of the MC model to simulate both the global and local behavior of the experimental wall test, as also highlighted in Pulatsu [58], this result is not included in the following sections where comparison of the prediction done by other numerical methods is discussed.

In conclusion, the proposed contact model was able to provide a relatively accurate representation of the mechanical behavior of masonry structures compared to the standard contact constitutive model typically used in DEM, with a negligible difference in computational efficiency in the overall numerical procedure.

5.6. Comparison to other numerical methods

The force-displacement curve for the proposed model shown in Fig. 20 is also compared against the results from numerical approaches proposed by other researchers. The comparison was only drawn to the selected numerical methods within the block-based modeling strategy. Fig. 26 shows the predictions made by the proposed model, the experimental results, and the numerical results reported by Pulatsu [58] and Pulatsu & Tuncay [80], Nie et al. [30], and Lourenço & Rots [27]. Nie et al. [30] did not report a comparison to the intermediate pre-compression stress (σ_v = 1.21 MPa). Hence, the comparison for the MID model is done only to the results reported by Pulatsu & Tuncay [80] and Lourenço & Rots [27].

It is evident on each pre-compression level that the responses from the proposed numerical model fall within the range of those reported by the other researchers [27,30,58,80]. The only exception is given for the test with low pre-compression by the model proposed by Nie et al. [30], where a premature stiffness reduction is obtained, followed by hardening before the final capacity drop due to toe crushing.

Even though Nie et al. [30], Lourenço & Rots [27], and the proposed model implemented the exponential softening law for tensile and shear with a slightly different implementation of exponential hardening/softening law in compression, the difference is apparent with regards to the global behavior of the wall models. This difference could be attributed to many factors, including the different modeling schemes (interface vs contact models), numerical implementations (implicit vs explicit), material input parameters, etc.

Meanwhile, the difference between the results reported by Pulatsu and Tuncay [80] could be attributed to the difference in the definition of the constitutive model and the one-way coupling scheme between

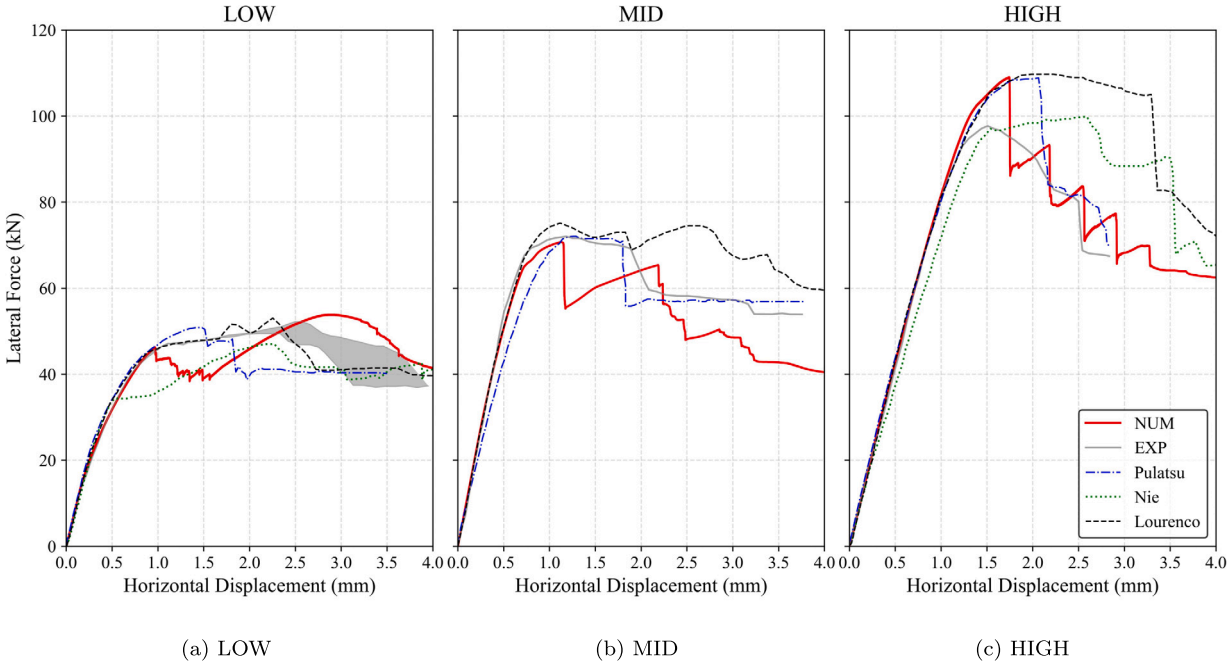

Fig. 26. Comparison of force-displacement response to other approaches in the literature.

Table 5
Comparison of peak load, displacement, and dissipated energy predictions.

			EXP	NUM	Pulatsu [58,80]	Nie et al. [30]	Lourenço & Rots [27]
LOW[a]	Peak Load	kN	52.23	53.74 (-2.89)	50.82 (2.70)	46.98 (10.06)	53.04 (-1.55)
	Peak Disp.	mm	2.49	2.91 (-16.47)	1.41 (43.31)	2.16 (13.40)	2.25 (9.81)
	Diss. Energy[b]	kN/mm	158.9	155.8 (1.99)	139.2 (12.44)	138.1 (13.10)	151.0 (4.97)
MID[a]	Peak Load	kN	72.03	70.70 (1.85)	72.05 (-0.01)	- (N/A)	75.15 (-4.32)
	Peak Disp.	mm	1.18	1.12 (4.89)	1.26 (-6.79)	- (N/A)	1.13 (5.43)
	Diss. Energy[b]	kN/mm	216.3	194.0 (10.28)	210.1 (2.85)	- (N/A)	235.9 (-9.1)
HIGH[a]	Peak Load	kN	97.69	109.10 (-11.58)	108.80 (-11.40)	99.89 (-2.24)	109.69 (-12.28)
	Peak Disp.	mm	1.51	1.74 (-15.62)	2.06 (-36.99)	2.58 (-71.77)	2.22 (-47.62)
	Diss. Energy[b]	kN/mm	199.9	206.8 (-3.47)	213.9 (-7.00)	208.9 (-4.51)	228.8 (-14.43)

[a] Values in brackets represent the percentage of relative error to experimental values.
[b] Dissipated energy calculated until the displacement at the end of the experiment.

shear and compression since both models were developed within the DEM framework.

The differences in the prediction of peak load, corresponding displacement, and dissipated energy on all compared approaches are quantified in Table 5. The dissipated energy, used to quantify the modeling accuracy in terms of pre-peak stiffness and post-peak strength degradations, was defined by calculating the area under the force-displacement curve. For a fair comparison, the energy calculated for each numerical method was limited until the corresponding displacement at the end of the experiment.

From Table 5, there seems to be no direct correlation between the peak load prediction from each numerical method and the applied pre-compression stress. Except for the Lourenço & Rots [27] model, the relative error for the peak load prediction of the proposed model and that made by Pulatsu [58,80] drops as the pre-compression stress increases from LOW to the MID model, but increases again from MID to the HIGH model.

These fluctuations could be influenced by many factors, including the inherent variability of the material properties in the walls compared to the values inputted in the numerical models and the representation of the potential crack surfaces in the brick units. In the LOW model, the splitting through the brick units was minimal as the failure mode was governed by the localized stair-stepped diagonal crack. The response of the brick units did not significantly affect the peak load prediction of the URM wall.

As the pre-compression increased to the MID model, the failure mode was still governed by the presence of the stair-stepped diagonal crack. Again, the peak load prediction was still unaffected by the mechanical behavior of the brick units. In contrast, in the HIGH model, the peak load prediction was governed by cracking occurring both through the brick units and the unit-mortar interfaces, with the former being predominant. Since this local failure is forced in the conducted simulations to occur in the mid-length of the brick units and it is associated with brittle post-peak strength degradation, its occurrence reduces the accuracy of the numerical predictions, such as in the case of the HIGH model.

Overall, it is evident that the proposed numerical strategy could predict the experimental responses within the 20% range of the experimental values. The predicted responses from the proposed strategy were also in agreement with the other numerical approaches.

6. Conclusions

This study introduces a robust contact constitutive model for the analysis of masonry structures using the distinct element method. The proposed constitutive model is developed under the block-based modeling strategy to predict the nonlinear mechanical responses of unreinforced masonry structures subjected to monotonic loading. The novelty

of this work includes the introduction of the multi-surface plasticity coupled with a hardening/softening law for the damage evolution in compression and the piecewise linear softening law in the shear and tension regions. A series of numerical simulations from the material level to a full-scale masonry wall test subjected to shear-compression loading was conducted to validate the proposed method. From the numerical validation results, it can be concluded that:

- The proposed contact model predicted the responses of the material tests in shear-compression, flexural, and pure compression with adequate accuracy, including the post-peak regime on each test.
- The simulation of two wall experiments subjected to in-plane lateral load and two levels of pre-compression loads showed a good agreement with the experimental results in terms of global (force-displacement curve) and local (damage pattern) behaviors of the masonry walls. The comparison of the force-displacement curve to other numerical methods in the literature within the block-based modeling strategy also indicated good and consistent predictions.
- The numerical damage pattern of the low (0.3 MPa) and intermediate (1.21 MPa) pre-compression model showed a localized diagonal crack with less crack through the bricks, while the high pre-compression model (2.12 MPa) showed a dispersed diagonal crack pattern with more cracks passing through the brick units. All models exhibited toe crushing at the end of the analysis, consistent with the experimental findings.
- The high-precompression model exhibited a stepwise force-displacement post-peak response due to cracks in the brick units that were 'forced' through the potential crack surfaces in the mid-length of the units.

As the future development of this research, the contact constitutive model will be extended to consider the stiffness degradation at the mortar joints and potential crack surfaces of the brick units in each damage regime, often observed in cyclic or seismic loading of unreinforced masonry structures. Different loading scenarios, e.g., out-of-plane loading, will also be considered to further exploit the capability of the proposed contact model and DEM in general. Moreover, the responses predicted by the numerical model could not fully represent the spatial variability of masonry properties due to the deterministic-based system. The variability of the material properties within the unreinforced masonry structures and the sensitivity to change in the values will also be explored in the future. Then, the potential crack surfaces in the brick units will also be refined into multiple plane orientations to represent smoother cracks through the brick units. Finally, the dilatancy softening at the onset of shear damage will also be considered as the future work of this research.

CRediT authorship contribution statement

Y.P. Oktiovan: Writing – original draft, Visualization, Software, Methodology, Formal analysis, Conceptualization. **F. Messali:** Writing – review & editing, Supervision, Resources, Project administration, Data curation. **B. Pulatsu:** Writing – review & editing, Validation, Software, Resources, Data curation. **J.V. Lemos:** Writing – review & editing, Validation, Software. **J.G. Rots:** Writing – review & editing, Visualization, Supervision, Project administration, Funding acquisition.

Declaration of competing interest

The authors declare that they have no known competing financial interests or personal relationships that could have appeared to influence the work reported in this paper.

Data availability

The data that support the findings of this study are available from the corresponding author, Y.P. Oktiovan, upon reasonable request.

Acknowledgement

The first author would like to acknowledge the support of Itasca for the provision of the *3DEC* software package through the Itasca Educational Partnership (IEP) Research Program.

References

[1] Dajun D. Studies on brick masonry under compression. Mater Struct 1997;30(4):247–52. https://doi.org/10.1007/BF02486183/METRICS.
[2] Parajuli RR. Features and seismic response of large masonry structures: a case study of Singh Durbar main building, Nepal. In: Masonry construction in active seismic regions. Woodhead Publishing. ISBN 9780128210871, 2021. p. 355–75.
[3] Russell AP, Ingham JM. Prevalence of New Zealand's unreinforced masonry buildings. Bull N Z Soc Earthq Eng 2010;43(3):182–201. https://doi.org/10.5459/bnzsee.43.3.182-201.
[4] Baquedano P, Eudave RR, Miranda FN, Graus S, Ferreira TM. Traditional earth construction in Latin America: a review on the construction systems and reinforcement strategies. In: Masonry construction in active seismic regions. Woodhead Publishing. ISBN 9780128210871, 2021. p. 99–121.
[5] D'Altri AM, Sarhosis V, Milani G, Rots J, Cattari S, Lagomarsino S, et al. Modeling strategies for the computational analysis of unreinforced masonry structures: review and classification. Arch Comput Methods Eng 2020;27(4):1153–85. https://doi.org/10.1007/s11831-019-09351-x.
[6] Davis L, Cogliano M, Casotto C, Grecchi G, Ozcebe S, Tsioli C, et al. Pragmatic seismic collapse meso-scale analysis of old Dutch masonry churches. Earthq Eng Struct Dyn 2023;53:622–45. https://doi.org/10.1002/EQE.4037.
[7] Bui TT, Limam A, Sarhosis V, Hjiaj M. Discrete element modelling of the in-plane and out-of-plane behaviour of dry-joint masonry wall constructions. Eng Struct 2017;136:277–94. https://doi.org/10.1016/J.ENGSTRUCT.2017.01.020.
[8] Oktiovan YP, Davis L, Wilson R, Dell'Endice A, Mehrotra A, Pulatsu B, et al. Simplified micro-modeling of a masonry cross-vault for seismic assessment using the distinct element method. Int J Archit Herit 2023. https://doi.org/10.1080/15583058.2023.2277328.
[9] D'Altri AM, de Miranda S, Castellazzi G, Sarhosis V. A 3D detailed micro-model for the in-plane and out-of-plane numerical analysis of masonry panels. Comput Struct 2018;206:18–30. https://doi.org/10.1016/J.COMPSTRUC.2018.06.007.
[10] Zhang S, Beyer K. Numerical investigation of the role of masonry typology on shear strength. Eng Struct 2019;192:86–102. https://doi.org/10.1016/J.ENGSTRUCT.2019.04.026.
[11] Addessi D, Sacco E, Paolone A. Cosserat model for periodic masonry deduced by nonlinear homogenization. Eur J Mech A, Solids 2010;29(4):724–37. https://doi.org/10.1016/J.EUROMECHSOL.2010.03.001.
[12] Pelà L, Cervera M, Roca P. An orthotropic damage model for the analysis of masonry structures. Constr Build Mater 2013;41:957–67. https://doi.org/10.1016/J.CONBUILDMAT.2012.07.014.
[13] Pelà L, Cervera M, Roca P. Continuum damage model for orthotropic materials: application to masonry. Comput Methods Appl Mech Eng 2011;200(9–12):917–30. https://doi.org/10.1016/J.CMA.2010.11.010.
[14] Saloustros S, Pelà L, Cervera M, Roca P. An enhanced finite element macro-model for the realistic simulation of localized cracks in masonry structures: a large-scale application. Int J Archit Herit 2018;12(3):432–47. https://doi.org/10.1080/15583058.2017.1323245.
[15] Milani G, Zuccarello FA, Olivito RS, Tralli A. Heterogeneous upper-bound finite element limit analysis of masonry walls out-of-plane loaded. Comput Mech 2007;40(6):911–31. https://doi.org/10.1007/S00466-006-0151-9/METRICS.
[16] Lagomarsino S, Penna A, Galasco A, Cattari S. TREMURI program: an equivalent frame model for the nonlinear seismic analysis of masonry buildings. Eng Struct 2013;56:1787–99. https://doi.org/10.1016/J.ENGSTRUCT.2013.08.002.
[17] Liberatore D, Addessi D. Strength domains and return algorithm for the lumped plasticity equivalent frame model of masonry structures. Eng Struct 2015;91:167–81. https://doi.org/10.1016/J.ENGSTRUCT.2015.02.030.
[18] Raka E, Spacone E, Sepe V, Camata G. Advanced frame element for seismic analysis of masonry structures: model formulation and validation. Earthq Eng Struct Dyn 2015;44(14):2489–506. https://doi.org/10.1002/EQE.2594.
[19] Vanin F, Penna A, Beyer K. Equivalent-frame modeling of two shaking table tests of masonry buildings accounting for their out-of-plane response. In: Frontiers in built environment 2020, vol. 6; 2020:519374.
[20] Siano R, Roca P, Camata G, Pelà L, Sepe V, Spacone E, et al. Numerical investigation of non-linear equivalent-frame models for regular masonry walls. Eng Struct 2018;173:512–29. https://doi.org/10.1016/J.ENGSTRUCT.2018.07.006.
[21] Chiozzi A, Milani G, Tralli A. A genetic algorithm NURBS-based new approach for fast kinematic limit analysis of masonry vaults. Comput Struct 2017;182:187–204. https://doi.org/10.1016/J.COMPSTRUC.2016.11.003.
[22] Iannuzzo A, Dell'Endice A, Van Mele T, Block P. Numerical limit analysis-based modelling of masonry structures subjected to large displacements. Comput Struct 2021;242:106372. https://doi.org/10.1016/j.compstruc.2020.106372.
[23] Block P, Lachauer L. Three-dimensional funicular analysis of masonry vaults. Mech Res Commun 2014;56:53–60. https://doi.org/10.1016/J.MECHRESCOM.2013.11.010.

[24] Block P, Ochsendorf J. Thrust network analysis: a new methodology for three-dimensional equilibrium. J Int Assoc Shell Spat Struct 2007;48(155):167–73.
[25] Fraternali F. A thrust network approach to the equilibrium problem of unreinforced masonry vaults via polyhedral stress functions. Mech Res Commun 2010;37(2):198–204. https://doi.org/10.1016/J.MECHRESCOM.2009.12.010.
[26] Hamid Lotfi BR, Benson Shing P. Interface model applied to fracture of masonry structures. J Struct Eng 1994;120(1):63–80. https://doi.org/10.1061/(ASCE)0733-9445(1994)120:1(63).
[27] Lourenço PB, Rots JG. Multisurface interface model for analysis of masonry structures. J Eng Mech 1997;123(7):660–8. https://doi.org/10.1061/(ASCE)0733-9399(1997)123:7(660).
[28] Oliveira DV, Lourenço PB. Implementation and validation of a constitutive model for the cyclic behaviour of interface elements. Comput Struct 2004;82(17–19):1451–61. https://doi.org/10.1016/J.COMPSTRUC.2004.03.041.
[29] Xie Z, Sousamli M, Messali F, Rots JG. A sub-stepping iterative constitutive model for cyclic cracking-crushing-shearing in masonry interface elements. Comput Struct 2021;257:106654. https://doi.org/10.1016/J.COMPSTRUC.2021.106654.
[30] Nie Y, Sheikh A, Visintin P, Griffith M. A robust computational strategy for failure prediction of masonry structures using an improved multi-surface damage-plastic based interface model. Int J Numer Methods Eng 2023;124(11):2498–528. https://doi.org/10.1002/NME.7218.
[31] van Zijl G. Modeling masonry shear-compression: role of dilatancy highlighted. J Eng Mech 2004;130(11):1289–96. https://doi.org/10.1061/(asce)0733-9399(2004)130:11(1289).
[32] Minga E, Macorini L, Izzuddin BA. A 3D mesoscale damage-plasticity approach for masonry structures under cyclic loading. Meccanica 2018;53(7):1591–611. https://doi.org/10.1007/S11012-017-0793-Z/FIGURES/25.
[33] Macorini L, Izzuddin BA. A non-linear interface element for 3D mesoscale analysis of brick-masonry structures. Int J Numer Methods Eng 2011;85(12):1584–608. https://doi.org/10.1002/nme.3046.
[34] Kumar N, Barbato M. New constitutive model for interface elements in finite-element modeling of masonry. J Eng Mech 2019;145(5):1–15. https://doi.org/10.1061/(ASCE)EM.1943-7889.0001592.
[35] Aref AJ, Dolatshahi KM. A three-dimensional cyclic meso-scale numerical procedure for simulation of unreinforced masonry structures. Comput Struct 2013;120:9–23. https://doi.org/10.1016/j.compstruc.2013.01.012.
[36] Karapitta L, Mouzakis H, Carydis P. Explicit finite-element analysis for the in-plane cyclic behavior of unreinforced masonry structures. Earthq Eng Struct Dyn 2011;40(2):175–93. https://doi.org/10.1002/EQE.1014. https://onlinelibrary.wiley.com/doi/full/10.1002/eqe.1014. https://onlinelibrary.wiley.com/doi/abs/10.1002/eqe.1014. https://onlinelibrary.wiley.com/doi/10.1002/eqe.1014.
[37] Pari M, Van de Graaf AV, Hendriks MA, Rots JG. A multi-surface interface model for sequentially linear methods to analyse masonry structures. Eng Struct 2021;238:112123. https://doi.org/10.1016/J.ENGSTRUCT.2021.112123.
[38] Oktiovan Y, Messali F, Rots J. Detailed distinct element modeling of a Utrecht wharf cellar for the assessment of the load-bearing capacity and failure mechanism. In: Topping B, Iványi P, Kruis J, editors. Proceedings of the seventeenth international conference on civil, structural and environmental engineering computing, vol. 6. Civil-Comp Press; 2023. p. 1–10.
[39] Pulatsu B, Erdogmus E, Lourenço PB, Lemos JV, Hazzard J. Discontinuum analysis of the fracture mechanism in masonry prisms and wallettes via discrete element method. Meccanica 2020;55(3):505–23. https://doi.org/10.1007/s11012-020-01133-1.
[40] Malomo D, DeJong MJ, Penna A. Distinct element modelling of the in-plane cyclic response of URM walls subjected to shear-compression. Earthq Eng Struct Dyn 2019;48(12):1322–44. https://doi.org/10.1002/eqe.3178.
[41] Lemos JV, Sarhosis V. Discrete element bonded-block models for detailed analysis of masonry. Infrastructures 2022;7(3):31. https://doi.org/10.3390/infrastructures7030031.
[42] Chen S, Bagi K. DEM analysis of masonry hemispherical domes externally reinforced with metal bars. Eng Struct 2023;291:116496. https://doi.org/10.1016/J.ENGSTRUCT.2023.116496.
[43] Cundall PA. Formulation of a three-dimensional distinct element model—Part I. A scheme to detect and represent contacts in a system composed of many polyhedral blocks. Int J Rock Mech Min Sci Geomech Abstr 1988;25(3):107–16. https://doi.org/10.1016/0148-9062(88)92293-0.
[44] Noh G, Bathe KJ. An explicit time integration scheme for the analysis of wave propagations. Comput Struct 2013;129:178–93. https://doi.org/10.1016/J.COMPSTRUC.2013.06.007.
[45] Manos P, Mehrotra A, Konstantatou M. Stability of scaffoldless dry stone vaults under microgravity and seismic loading. In: Gabriele S, Manuello Bertetto A, Marmo F, Micheletti A, editors. Shell and spatial structures. Cham: Springer Nature Switzerland. ISBN 978-3-031-44328-2, 2024. p. 522–31.
[46] Lee JH, Li C, Oh SH, Yang WJ, Yi WH. Evaluation of rocking and toe crushing failure of unreinforced masonry walls. Adv Struct Eng 2008;11(5):475–89. https://doi.org/10.1260/136943308786411998.
[47] Pulatsu B, Gonen S, Lourenço PB, Lemos JV, Hazzard J. Computational investigations on the combined shear–torsion–bending behavior of dry-joint masonry using DEM. Comput Part Mech 2023;10(2):249–60. https://doi.org/10.1007/S40571-022-00493-7/TABLES/3.
[48] Itasca Consulting Group Inc.. 3DEC - three dimensional distinct element code ver. 7.0; 2013.
[49] Cundall P, Detournay C. Dynamic relaxation applied to continuum and discontinuum numerical models in geomechanics. Rock Mech Eng 2017:45–90. https://doi.org/10.1201/B20402-2.
[50] Lemos JV, Bagi K. Discrete element modeling, Chap. 4. Cham: Springer Nature Switzerland. ISBN 978-3-031-32476-5, 2023. p. 189–232.
[51] Belytschko T. An overview of semidiscretization and time integration procedures. In: Belytschko T, Hughes T, editors. Computational methods for transient analysis. New York: Elsevier Science Publisher; 1983. p. 1–65.
[52] Smolinski P. Stability analysis of a multi-time step explicit integration method. Comput Methods Appl Mech Eng 1992;95(3):291–300. https://doi.org/10.1016/0045-7825(92)90188-P.
[53] Smolinski P, Sleith S, Belytschko T. Stability of an explicit multi-time step integration algorithm for linear structural dynamics equations. Comput Mech 1996;18:236–44.
[54] Sarhosis V, Lemos JV. A detailed micro-modelling approach for the structural analysis of masonry assemblages. Comput Struct 2018;206:66–81. https://doi.org/10.1016/j.compstruc.2018.06.003.
[55] Sarhosis V, Oliveira DV, Lemos JV, Lourenco PB. The effect of skew angle on the mechanical behaviour of masonry arches. Mech Res Commun 2014;61:53–9. https://doi.org/10.1016/J.MECHRESCOM.2014.07.008.
[56] Godio M, Stefanou I, Sab K. Effects of the dilatancy of joints and of the size of the building blocks on the mechanical behavior of masonry structures. Meccanica 2018;53(7):1629–43. https://doi.org/10.1007/S11012-017-0688-Z/FIGURES/19.
[57] Esposito R, Ravenshorst GJ. Quasi-static cyclic in-plane tests on masonry components 2016/2017. Delft University of Technology Report. 2017:C31B67WP3-4.
[58] Pulatsu B. Coupled elasto-softening contact models in DEM to predict the in-plane response of masonry walls. Comput Part Mech 2023;10:1759–70. https://doi.org/10.1007/s40571-023-00586-x.
[59] Andreotti G, Graziotti F, Magenes G. Detailed micro-modelling of the direct shear tests of brick masonry specimens: the role of dilatancy. Eng Struct 2018;168:929–49. https://doi.org/10.1016/J.ENGSTRUCT.2018.05.019.
[60] Chaimoon K. Numerical simulation of fracture in unreinforced masonry. Ph.D. thesis. Sydney: University of New South Wales; 2007.
[61] Li Y, Zeng B. Modeling of masonry structures using a new 3D cohesive interface material model considering dilatancy softening. Eng Struct 2023;277:115466. https://doi.org/10.1016/J.ENGSTRUCT.2022.115466.
[62] Mann W, Muller H. Failure of shear stressed masonry. An enlarged theory, tests and application to shear walls. Proc Br Ceram Soc 1982;30:223–35.
[63] Pulatsu B, Gonen S, Erdogmus E, Lourenço PB, Lemos JV, Prakash R. In-plane structural performance of dry-joint stone masonry Walls: a spatial and non-spatial stochastic discontinuum analysis. Eng Struct 2021;242:112620. https://doi.org/10.1016/J.ENGSTRUCT.2021.112620.
[64] van der Pluijm R. Out-of-plane bending of masonry: behaviour and strength. Phd thesis 1 (research tue / graduation tue). Built Environment; 1999.
[65] Jafari S, Rots JG, Esposito R. Core testing method to assess nonlinear behavior of brick masonry under compression: a comparative experimental study. Constr Build Mater 2019;218:193–205. https://doi.org/10.1016/J.CONBUILDMAT.2019.04.188.
[66] Vermeltfoort A. Brick-mortar interaction in masonry under compression. Phd thesis 1 (research tue / graduation tue). Built Environment; 2005.
[67] Esposito R, Messali F, Rots JG. Tests for the characterization of replicated masonry and wall ties; 2016. http://resolver.tudelft.nl/uuid:a0923cf9-0ccd-48a1-9ce1-082aa66e97af.
[68] Lourenco P. Computational strategies for masonry structures. Ph.D. thesis. Delft University of Technology; 1996. https://repository.tudelft.nl/islandora/object/uuid%3A4f5a2c6c-d5b7-4043-9d06-8c0b7b9f1f6f.
[69] Gooch LJ, Masia MJ, Stewart MG, Lam CY. Statistical assessment of tensile and shear properties of unreinforced clay brick masonry. Constr Build Mater 2023;386:131578. https://doi.org/10.1016/J.CONBUILDMAT.2023.131578.
[70] Messali F, Esposito R, Ravenshorst G, Rots J. Experimental investigation of the in-plane cyclic behaviour of calcium silicate brick masonry walls. Bull Earthq Eng 2020;18(8):3963–94. https://doi.org/10.1007/s10518-020-00835-x.
[71] Korswagen PA, Longo M, Rots JG. Calcium silicate against clay brick masonry: an experimental comparison of the in-plane behaviour during light damage. Bull Earthq Eng 2020;18(6):2759–81. https://doi.org/10.1007/S10518-020-00803-5/TABLES/3.
[72] Jafari S, Rots JG, Esposito R. A correlation study to support material characterisation of typical Dutch masonry structures. J Build Eng 2022:45. https://doi.org/10.1016/j.jobe.2021.103450.
[73] EN 1052-1. Method of test masonry – part 1: determination of compressive strength. Tech. Rep.. Nederlands Normalisatie-Instituut; 1999.
[74] Gonen S, Pulatsu B, Erdogmus E, Lourenço PB, Soyoz S. Effects of spatial variability and correlation in stochastic discontinuum analysis of unreinforced masonry walls. Constr Build Mater 2022;337:127511. https://doi.org/10.1016/J.CONBUILDMAT.2022.127511.
[75] Müller D, Förster V, Graubner CA. Influence of material spatial variability on required safety factors for masonry walls in compression. Mauerwerk 2017;21(4):209–22. https://doi.org/10.1002/DAMA.201700004.

[76] Pulatsu B, Gonen S, Parisi F, Erdogmus E, Tuncay K, Funari MF, et al. Probabilistic approach to assess URM walls with openings using discrete rigid block analysis (D-RBA). J Build Eng 2022;61:105269. https://doi.org/10.1016/J.JOBE.2022.105269.
[77] Vermeltfoort A, Raijmakers T, Janssen H. Shear tests on masonry walls. In: Hamid A, Harris H, editors. 6th North American masonry conference. Technomic Publ. Co.; 1993. p. 1183–93, ISBN 84-0751591.
[78] Chaimoon K, Attard MM. Modeling of unreinforced masonry walls under shear and compression. Eng Struct 2007;29(9):2056–68. https://doi.org/10.1016/J.ENGSTRUCT.2006.10.019.
[79] Jafari S. Material characterisation of existing masonry: a strategy to determine strength, stiffness and toughness properties for structural analysis. Ph.D. thesis. Delft: Delft University of Technology; 2021.
[80] Pulatsu B, Tuncay K. Computational modeling of damage progression in unreinforced masonry walls via DEM. Turk J Civil Eng 2023. https://doi.org/10.18400/tjce.1323977.
[81] De Borst R, Wells GN, Sluys LJ. Some observations on embedded discontinuity models. Eng Comput (Swans, W) 2001;18(1–2):241–54. https://doi.org/10.1108/02644400110365897/FULL/XML.